Delft University of Technology

Morphodynamic Modeling of Tidal Basins
The Role of Sand-Mud Interaction

Colina Alonso, A.; van Maren, D. S.; van Weerdenburg, R. J.A.; Huismans, Y.; Wang, Z. B.

Important note
To cite this publication, please use the final published version (if applicable).
Please check the document version above.

Morphodynamic Modeling of Tidal Basins: The Role of Sand-Mud Interaction

A. Colina Alonso[1,2] ⬥, D. S. van Maren[1,2,3] ⬥, R. J. A. van Weerdenburg[2] ⬥, Y. Huismans[1,2] ⬥, and Z. B. Wang[1,2] ⬥

[1]Faculty of Civil Engineering and Geosciences, Delft University of Technology, Delft, The Netherlands, [2]Department of Marine and Coastal Systems, Deltares, Delft, The Netherlands, [3]State Key Lab of Estuarine and Coastal Research, East China Normal University, Shanghai, China

Abstract The morphology of tide-dominated systems is progressively influenced by human activities and climate change. Quantitative approaches aiming at understanding or forecasting the effects of interventions and climate change are often aggregated, thereby simplifying or schematizing the investigated area. In this work, we advance on the knowledge of sediment transport processes shaping tidal systems and on methodologies translating schematized model output into physically realistic variables. In terms of improved physics, we systematically evaluate the influence of sand-mud interaction processes. Most tidal systems are shaped by a mixture of sand and mud. Morphological models typically compute transport of sand and mud independently, despite studies clearly demonstrating that their physical behavior is mutually dependent. We investigate the effects of two interaction mechanisms (erosion interaction and roughness interaction, applied with varying mud erodibility) with a schematized process-based morphodynamic model. We convert model output into metrics that describe the meso-scale configuration of the modeled systems, allowing a quantitative comparison of scenarios. Modeled patterns and intertidal flat shape, size and composition widely vary with mud erodibility settings, but equally depend on the evaluated sand-mud interaction mechanisms (with erosion interaction having a larger effect than roughness interaction). Sand-mud interaction thus needs to be accounted for from a physical point of view, but also to improve predictions of tidal basin evolution models, particularly the (bimodally distributed) sediment composition of intertidal flats.

Plain Language Summary Human interventions and climate change are progressively influencing the state of coastal systems. Their impact on coastal evolution takes place on decades to centuries and the present-day modeling tools have limitations to study these impacts. Models with highly schematized configurations have often been used in the past to increase our understanding of coastal evolution. We advance on this, by determining the effect of sand-mud interaction on the modeled long-term evolution of tidal basins. The bed of most tidal basins is composed of two sediment types: sand and mud. From previous research, it is known that sand and mud do not behave independently. We investigate the effects of two interaction mechanisms (erosion and roughness interaction) using a model with a schematized configuration in terms of topology and forcing, but including the most relevant physical processes. To quantitatively compare the output of different model scenarios, we translate the results into a number of metrics. Our results reveal that sand-mud interaction processes (particularly erosion interaction) influence tidal basin evolution. Including sand-mud interaction can significantly improve modeling results, especially the sediment composition of intertidal flats. We present guidelines that can be followed to improve models depending on the real-life system they should compare to.

1. Introduction

Worldwide, deltas are under pressure from climate change and increasing human activities, undergoing transitions in their abiotic and biotic systems (e.g., Syvitski et al., 2009). Anthropogenic interferences in estuaries and tidal basins can irreversibly influence their morphological development and threaten their existence (Dijkstra et al., 2019; Wang et al., 2015). In addition, climate change introduces a new spectrum of coastal challenges, such as coping with sea level rise (SLR), increased storminess and saltwater intrusion (IPCC, 2022). To face these existential threats and protect our deltas, we must gain a thorough understanding of the effects of climate change, as well as of the effectiveness and potential side-effects of mitigating measures such as coastal interventions.

Investigation: A. Colina Alonso, D. S. van Maren, R. J. A. van Weerdenburg, Z. B. Wang

Methodology: A. Colina Alonso, D. S. van Maren, R. J. A. van Weerdenburg, Y. Huismans

Project Administration: D. S. van Maren, Z. B. Wang

Resources: A. Colina Alonso

Software: A. Colina Alonso, D. S. van Maren, R. J. A. van Weerdenburg

Supervision: D. S. van Maren, Y. Huismans, Z. B. Wang

Validation: A. Colina Alonso

Visualization: A. Colina Alonso, D. S. van Maren

Writing – original draft: A. Colina Alonso

Writing – review & editing: D. S. van Maren, R. J. A. van Weerdenburg, Y. Huismans, Z. B. Wang

Morphodynamic effects of climate change and human interventions play a role on decadal to centennial timescales. Forecasting the morphological impact requires numerical tools that can handle such long timescales. However, model complexity and simulation periods are coupled. Long forecasting periods require simplified model configurations because of error propagation (Hajek et al., 2012), the associated computational time, and the requirement of morphodynamic equilibrium (Hoitink et al., 2020). In the context of climate change, especially this latter requirement is very relevant because morphological adjustment to SLR introduces subtle variations in sediment transport. When the timescale related to the investigated changes (T_c) is smaller than the time required for the model to attain morphodynamic equilibrium (T_e) the model is still spinning up, overwhelming the small variations introduced by for example, SLR.

A solution to use complex numerical models while satisfying $T_c > T_e$ is to use highly schematized configurations in which the topography and the forcing are largely simplified. Moreover, simplified schematizations are more suitable to study morphodynamic mechanisms in isolation, compared to models with realistic but also inherently complex geometries and boundary conditions. Such simplified models have advanced our understanding of the meso-scale coastal evolution of deltas on large timescales. Initially, these studies focused on the dynamics of sandy coasts only (e.g., Dissanayake et al., 2009; Guo et al., 2015; Hibma et al., 2003; Marciano et al., 2005; van der Wegen & Roelvink, 2008). However, real tidal systems are often shaped by a mixture of sand and mud. A number of follow-up studies were extended with mud-sized sediment to improve the prediction of large-scale delta evolution (Caldwell & Edmonds, 2014; Edmonds & Slingerland, 2010; Geleynse et al., 2011) and of intertidal flat formation (e.g., Braat et al., 2017; Elmilady et al., 2020, 2022). These existing studies so far largely treated sand and mud as independent fractions, despite overwhelming evidence that erosion of sand and mud is mutually coupled (Jacobs, 2011; Torfs, 1995; van Ledden, 2003; van Rijn, 2020). Besides, the substrate introduces complex feedback mechanisms related to hydraulic roughness—which can be lower in muddy beds, thereby promoting deposition of mud (Soulsby & Clarke, 2005)—and to biologic activity. An example of the latter is that intertidal benthic algae prefer a muddy substrate, and once in place facilitate more net mud deposition (see e.g., Brückner et al., 2021; Grabowski et al., 2011; van der Wal et al., 2010). Although some of these complexities have been addressed in numerical models (Brückner et al., 2021; Le Hir et al., 2011; van Ledden, Wang, et al., 2004), their inclusion in long-term prediction models remains limited. As a result, despite advances in our understanding of small-scale sand-mud interaction processes, their large-scale morphological implications still remain poorly understood.

In this study we aim at a better understanding of the effects of including small-scale sand-mud interaction on modeled large-scale morphodynamics of tidal basins. We focus on abiotic interactions, since the increasing complexity arising from biotic effects (Brückner et al., 2021; X. Chen et al., 2021; Grabowski et al., 2011; Herman et al., 2001) may obscure the abiotic interactions which are already complex themselves. We study long-term tidal basin evolution with a schematized model inspired by the tidal basins in the Dutch Wadden Sea, in which two sand-mud interactions have been implemented. An important drawback of such schematized configurations is that it is difficult to correlate simplified model layouts with real world issues. A key challenge is how to capture the fundamental aspects of real-world systems in low complexity models, and how to quantitatively validate the schematized model performance. We therefore introduce metrics to correlate the range of model realizations resulting from sand-mud interaction mechanisms with the real world.

The structure of this paper is as follows: We first introduce the theory of the two studied sand-mud interaction mechanisms in Section 2. In Section 3, we present our modeling methodology and the implementation of the sand-mud interaction mechanisms. The model results in which we analyze 50 years of basin evolution under different model settings are presented in Section 4. Here, we also compare them with field data from the Wadden Sea. In Section 5 we discuss our results, focusing on the large-sale impact of sand-mud interaction and on the opportunities it provides to improve morphodynamic modeling. Lastly, conclusions are given in Section 6.

2. Theory on Abiotic Sand-Mud Interaction Mechanisms

2.1. Interdependent Erosion

Sand-mud mixtures can be non-cohesive or cohesive, depending on the small-scale structure of the sediment bed (two regimes, see Figure 1a). When clay contents are below a critical amount ($p_{clay,crit}$), the internal structure is determined by the inter-particle locking of sand grains and the mixture can be treated as non-cohesive sediment.
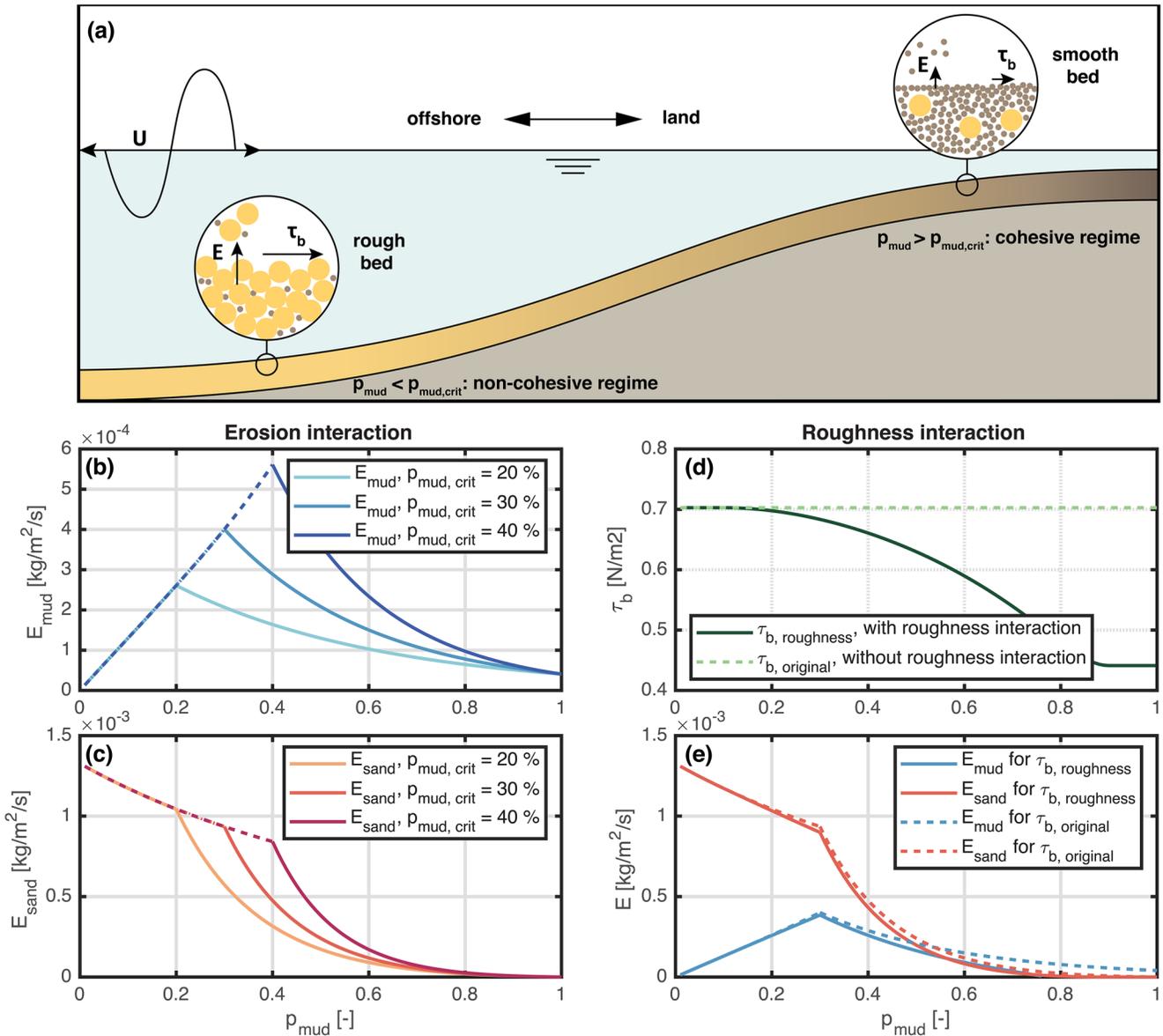
Figure 1. (a) Sketch illustrating sediment erosion and bed roughness for different sand-mud content. (b and c) Erodibility feedback: Relation between the erosion rate of mud and sand and the mud content, based on van Ledden ([2003]) for several values of $p_{mud,crit}$. (d and e) Roughness feedback: Bed shear stresses decrease with increasing mud content, hence decreasing erosion rates. $\tau_{b,original}$ refers to the bed shear stresses calculated without accounted for roughness interaction. Panels (b–e) are calculated for the conditions: $U = 0.75$ m/s, $h = 5$ m, $\tau_{e,mud} = 0.5$ Pa, $M_e = 10^{-4}$ m/s, $D_{50,sand} = 150$ μm. A gradual transition is imposed between rough beds ($k_s = k_{s,sand}$) and smooth beds ($k_s = k_{s,silt}$) at $0.1 < p_m < 0.9$.

At $p_{clay,crit}$, sand grains lose contact and they become part of a mud matrix in which clay cohesion determines the structure (Jacobs et al., [2011]; Torfs, [1995]; van Ledden, van Kesteren, & Winterwerp, [2004]). This critical clay content is a function of the sand grain size, the type of cohesive material, the water content and the organic content. The transition between the two regimes takes place at $p_{clay,crit}$ of 5%–10% (van Ledden, van Kesteren, & Winterwerp, [2004]). Assuming a constant clay/silt ratio, which is a reasonable assumption for cohesive sediments in the considered tidal and estuarine systems (Colina Alonso et al., [2022]; van Ledden, van Kesteren, & Winterwerp, [2004]), a critical mud content ($p_{mud,crit}$) can be determined at which the transition takes place ($p_{mud,crit} \approx 0.3$ for the considered systems). Herein, mud is defined as all sediment with a grain size smaller than 63 μm (i.e., silt and clay).

The erosion behavior of sand-mud mixtures has been the topic of experimental studies (e.g., Jacobs, [2011]; Mitchener & Torfs, [1996]; van Rijn, [2020]) and has been numerically parameterized (e.g., Le Hir et al., [2011];

van Ledden, 2003). From experimental and theoretical studies it follows that the erosion fluxes of sand and mud are proportionally coupled with erosion of both sand and mud depending on the erosion properties of the non-cohesive or cohesive mixture (D. Chen et al., 2021; Jacobs et al., 2011; Le Hir et al., 2011; Mitchener & Torfs, 1996; van Ledden, van Kesteren, & Winterwerp, 2004; Winterwerp & van Kesteren, 2004). Non-cohesive erosion can thus be parameterized with sand transport formulations such as van Rijn (1993); cohesive erosion with a Partheniades-type equation. Following this parametrization, we illustrate the erosion rates as a function of mud content (computed with van Ledden (2003)'s model, which we will use in Section 3.2) in Figures 1b and 1c.

2.2. Hydraulic Roughness of the Bed

The sediment composition also affects the hydraulic roughness of the bed, which can largely impact effective bed shear stresses and erosion rates. The hydraulic roughness consists of a form drag component (resulting from bed forms) and a skin friction component (resulting from the grain size of the bed). Water-bed exchange processes are determined by a thin layer near the bed depending on skin friction rather than form drag, whereas the large-scale flows depend on the form drag (Winterwerp et al., 2021). The hydraulic roughness (skin friction) of mud beds is lower than that of sand beds, because larger sand grains generate more near-bed turbulence. Since the bed shear stress increases with the hydraulic roughness, and assuming the depth-averaged flow is not or only limitedly influenced by the small-scale skin roughness, lower bed shear stresses will be exerted on muddy beds (Yao et al., 2018). An increase in the mud content of the bed therefore weakens the erosion forces.

Assuming that the hydrodynamic roughness influencing water-bed exchange of sediment is primarily influenced by skin friction (as above), the effect of the mud content on the bed shear stress can be computed using the method of Soulsby and Clarke (2005) (see Figure 1d for the bed shear stress with this effect in dark green and without this effect in dashed light green). The reduction of the bed shear stress has a notable effect on the sand and mud erosion fluxes, as illustrated in the example of see Figure 1e (which is calculated using the formulations of van Ledden (2003) with $p_{mud,crit} = 0.3$): The erosion fluxes are lower for higher mud contents, which already follows from van Ledden (2003), but this is substantially strengthened when accounting for bed roughness effect, especially in the cohesive domain. In the example of Figure 1, the mud erosion fluxes are even reduced to 0 for very muddy sediments ($p_{mud} > 0.7$) for the considered hydrodynamic conditions.

3. Methods

3.1. Numerical Model Set-Up

We explore the effects of erodibility interaction and roughness interaction (as defined in Section 2) on tidal basin evolution using a depth-averaged (2DH) Delft3D morphodynamic model (version 6.03.00.59659, see also Lesser et al., 2004). We have developed a schematized model of a tidal basin instead of a realistic case, because such a schematized basin is minimally restricted by initial topography or bed sediment—which would otherwise strongly influence the model outcome (see e.g., Dastgheib et al., 2008; Rahdarian et al., 2022).

The schematized configuration of the tidal basin is based on the tidal basins of the Wadden Sea. The model domain consists of a tidal inlet in between two islands and a back-barrier basin with dimensions of 15×10 km. The computational grid is regular with a resolution of 100×100 m. We work with a stratified bed consisting of an active transport top layer with a thickness of 0.1 m and 20 Eulerian bed layers with a thickness of 1 m underneath. Starting from a sloping bathymetry and a uniform sediment composition ($p_{sand} = 0.95$, $p_{mud} = 0.05$), basin evolution is simulated for a period of 50 years. Within this period, its morphological and sedimentological state converges to a dynamic equilibrium. The model is forced by a semi-diurnal tide with an amplitude of 1.5 m (S2 + S4) entering from the (only) open boundary at the North (located 15 km from the inlet), and a wave-climate created by locally generated wind-waves of varying strength (with wind speeds of 4–8 m/s) and direction (SW-NW). Flow and wave calculations are coupled online during the simulation, such that there is a two-way wave-current interaction. In the sediment transport module, the bed shear stresses under combined currents and waves are computed according to Soulsby and Clarke (2005) while we assume the hydrodynamics to be driven by a form roughness independent of the sediment type. The mud concentration at the offshore (Northern) open boundary is set to 5 mg/l, which is representative for offshore concentrations in the North Sea.

Simulations are carried out with one medium fine sand fraction ($D_{50} = 250$ μm) and one mud fraction. The form roughness height driving hydrodynamics is set at $k_{s,hydro} = 0.02$ m (typical for bedforms in sandy systems, see

Table 1
Model Parameter Settings

Parameter	Value	Description
a	1.5	Tidal amplitude (m)
$k_{s,hydro}$	2e−2	Bedform-related roughness height for hydrodynamic calculations (m)
$k_{s,sand}$	6e−4	Nikuradse roughness height (skin friction) for pure sand (m)
$k_{s,silt}$	3e−5	Nikuradse roughness height (skin friction) for pure mud (m)
MorFac	50	Morphological scale factor (-)
D_{50}	250	Median grain diameter of sand (μm)
w_s	2.5e−4	Settling velocity of mud (m/s)
τ_e	0.125–2	Critical bed shear stress for erosion of mud (N/m²)
M	1e−4	Erosion parameter (m/s)
$p_{mud,crit}$	0.3	Critical mud content for cohesive behavior (−)
β_m	1	Bed packing coefficient (−)
$c_{mud,bound}$	5	Suspended mud concentration at the boundary (mg/l)

e.g., van Rijn (1993)), and is independent of the sediment type (see section on roughness interaction for the bed roughness driving erosion of the bed). The type of mud differs between scenarios, ranging from mud that is easily eroded (τ_e = 0.125 Pa) to consolidated mud (τ_e = 2.0 Pa). For simulations not accounting for sand-mud erosion interaction, sand transport is calculated with the Van Rijn transport formulations (van Rijn, 1993) and mud transport with the Partheniades erosion formulation (Partheniades, 1965) and a gross deposition flux depending on the suspended mud concentrations and settling velocity (Sanford & Halka, 1993; Winterwerp, 2007). Details on the implementation of sand-mud interaction are provided in Section 3.2. Computational times were not affected when including sand-mud interaction in the model simulations. Basic model settings are summarized in Table 1; model scenarios to explore the effect of sand-mud interaction in Table 2. For additional information on the model set-up, we refer to Supporting Information S1.

3.2. Implementation of Sand-Mud Interaction Mechanisms

3.2.1. Erosion Interaction

We follow the sand-mud erosion formulations by van Ledden (2003), using $p_{mud,crit}$ = 0.3 (see also van Ledden, Wang, et al. (2004), van Ledden et al. (2006), and Section 2.1). In the non-cohesive regime ($p_{mud} < p_{mud,crit}$), sand erosion (E_{sand}) is calculated using the sand entrainment formulation of van Rijn (1993). Although the sediment mixture is non-cohesive, the presence of small amounts of mud does slightly influence the critical bed shear stress for erosion. This is accounted for as follows:

$$\tau_{e,nc}/\tau_{cr} = (1 + p_{mud})^{\beta_m}, \tag{1}$$

in which $\tau_{e,nc}$ is the critical shear stress for non-cohesive mixtures, τ_{cr} is the critical shear stress for pure sand, p_{mud} is the mud content at the bed surface and β_m is an empirical coefficient (ranging from 0.75 to 1.25) which depends on the packing of the bed (van Ledden, 2003). Sand erosion fluxes (E_{sand}) are calculated following:

$$E_{sand} = \frac{\alpha_{b1}}{3}\frac{\sqrt{\Delta g D_{50}}}{D_*^{0.9}}T_{nc}^{\alpha_{b2}-0.9}, \tag{2}$$

in which α_{b1} and α_{b2} are coefficients depending on the transport parameter T_{nc} (α_{b1} = 0.053, α_{b2} = 2.1 for T < 3 and α_{b1} = 0.1, α_{b2} = 1.5 for T ≥ 3), Δ is the specific gravity of sand, g is the gravitational acceleration, D_{50} is the median

Table 2
Model Scenarios, Executed With τ_e = 2 Pa, τ_e = 1 Pa, τ_e = 0.5 Pa, τ_e = 0.25 Pa, and τ_e = 0.125 Pa

τ_e	Erosion interaction	Roughness interaction
x	No	No
x	Yes	No
x	No	Yes
x	Yes	Yes

Note. No erosion interaction means that erosion of sand and mud are calculated independently following the van Rijn (1993) and Partheniades (1965) formulations respectively. When erosion interaction is included, sand and mud erosion are calculated following van Ledden (2003). When accounting for roughness interaction, the roughness height used to calculate the skin-friction (thus also the erosion bed shear stress) depends on the mud content in the bed. Otherwise, this value is independent of the sediment composition (see also Section 3.2).

sand grain size and D_* is the dimensionless grain size. T_{nc} includes the bed shear stress for non-cohesive mixtures (see also Equation 1) and is defined as:

$$T_{nc} = \frac{\tau_b}{\tau_{e,nc}} - 1 = \frac{\tau_b}{\tau_{cr}(1 + p_{mud})^{\beta_m}} - 1, \tag{3}$$

in which τ_b is the bed shear stress.

Mud erosion fluxes (E_{mud}) are proportional to the calculated sand erosion fluxes following:

$$\frac{E_{mud}}{E_{sand}} = \frac{p_{mud}}{p_{sand}} = \frac{p_{mud}}{1 - p_{mud}}. \tag{4}$$

Therefore, they follow the following relation in the non-cohesive regime:

$$E_{mud} = \frac{p_{mud}}{1 - p_{mud}} \frac{\alpha_{b1}}{3} \frac{\sqrt{\Delta g D_{50}}}{D_*^{0.9}} T_{nc}^{\alpha_{b2}-0.9}. \tag{5}$$

The reader is referred to van Ledden (2003) for the derivation of Equations 2–5.

In the cohesive regime ($p_{mud} \geq p_{mud,crit}$), E_{sand} and E_{mud} are both computed with a Partheniades-type of equation, stating that above a certain critical bed shear stress the cohesive bed starts to erode with an erosion rate M_c. Following van Ledden (2003), the erosion formulations for both sediment types are as follows:

$$E_{sand} = (1 - p_{mud})M_c\left(\frac{\tau_b}{\tau_{e,c}} - 1\right)H\left(\frac{\tau_b}{\tau_{e,c}} - 1\right), \tag{6}$$

$$E_{mud} = p_{mud} M_c\left(\frac{\tau_b}{\tau_{e,c}} - 1\right)H\left(\frac{\tau_b}{\tau_{e,c}} - 1\right), \tag{7}$$

in which $H\left(\frac{\tau_b}{\tau_{e,c}} - 1\right)$ is a Heaviside function that equals 1 when the argument is larger than 0 and equals 0 when the argument is less or equal to 0. $\tau_{e,c}$ is the critical erosion shear stress for cohesive sand-mud mixtures, and is linearly interpolated between $\tau_{e,nc}$ (the critical bed shear stress for the non-cohesive regime) and τ_e (the critical bed shear stress for a pure mud bed):

$$\tau_{e,c} = \frac{\tau_{cr}(1 + p_{m,cr})^\beta - \tau_e}{1 - p_{m,cr}}(1 - p_m) + \tau_e. \tag{8}$$

The expression for the cohesive erosion coefficient reads:

$$\log(M_c) = \frac{\log\left(\frac{M_{nc}}{1 - p_{mud,crit}}\right) - \log(M)}{1 - p_{mud,crit}}(1 - p_{mud}) + \log(M), \tag{9}$$

in which M is the erosion coefficient for a pure mud bed, which in reality can range from 10^{-3} to 10^{-5} kg/m²/s (Winterwerp & van Kesteren, 2004). M_{nc} is the erosion coefficient for non-cohesive mixtures, defined as:

$$M_{nc} = \frac{\alpha_{\beta1}}{3} \frac{\sqrt{\Delta g D_{50}}}{D_*^{0.9}}. \tag{10}$$

The drawback in this approach is that for multiple sand and mud fractions it becomes mathematically complex, since each fraction may have its own value for M_c and M_{nc}. Even though our model simulations only contain one mud and one sand fraction, we apply the more generic modification of van Kessel et al. (2012), in which the erosion rate itself is interpolated instead of $\tau_{e,c}$ and M_c separately (but which results in very similar E_{mud} values). The erosion flux then reads:

$$E_{mud,i} = E_{f,mud,i}\left(\frac{E_{s,mud,i}}{E_{f,mud,i}}\right)^{\frac{1-p_{mud}}{1-p_{mud,crit}}}, \tag{11}$$

where $E_{mud,i}$ is the erosion velocity of mud within the cohesive mixture for fraction i, $E_{f,mud,i}$ is the erosion velocity of pure mud for mud fraction i, and $E_{s,mud,i}$ is the erosion velocity for mud fraction i in the non-cohesive regime (based on Equation 5).

3.2.2. Roughness Interaction

We calculate the effect of the mud content on the hydraulic roughness close to the bed, and consequently on the bed shear stress driving sediment erosion, using the method of Soulsby and Clarke (2005). Here we focus on the aspects of their methodology that relate to the sediment composition, but we refer to Soulsby and Clarke (2005) for a complete overview of their method.

In case of hydrodynamically rough turbulent flows, the bed roughness (z_0) depends on the surface texture of the sediment bed. Following Soulsby and Clarke (2005), a representative grain size (D_{50}) of the sediment is used as a measure for the surface texture such that:

$$z_0 = D_{50}/12. \tag{12}$$

Herein, they assume that

$$k_s = 2.5 D_{50}. \tag{13}$$

The dependency of the bed roughness on the grain size implies that the bed roughness is adjusted for changes in sediment composition, such that the bed roughness decreases with an increasing mud fraction (and vice versa). Since the characteristic grain size diameter D_{50} is not a dependent variable in the Delft3D modeling suite, a slightly different alternative to Equation 12 has been implemented. Following Equations 12 and 13, z_0 is determined as:

$$z_0 = k_s/30. \tag{14}$$

We define $k_{s,silt}$ as the roughness height (in [m]) for a mud-dominated sediment bed and $k_{s,sand}$ as the roughness height (in [m]) for a sand-dominated sediment bed. k_s is thus implemented as a Nikuradse roughness height depending on the sediment grain size (Equation 13) and it switches between $k_{s,silt}$ (0.03 mm) and $k_{s,sand}$ (0.6 mm) depending on the mud content (see Figure 1d and Table 1). We have introduced a gradual transition in between to better represent actual physical conditions and avoid numerical instabilities.

4. Results

4.1. Phenomenological Description

We first evaluate the model results by comparing the morphodynamic evolution in terms of bed morphology and spatial mud distribution (Figure 2). All model scenarios generate an intricate pattern of tidal channels and flats, where in general the mud content increases in landward direction. Yet, both the bathymetry and the bed composition largely vary depending on the mud erosion settings and the interaction mechanisms.

Erosion interaction most strongly influences morphology for simulations with poorly erodible mud ($\tau_e = 1.00$ Pa, $\tau_e = 2.00$ Pa, see Figure 2). Without this interaction mechanism, mud is too immobile to be eroded from the channels, resulting in a morphology with large, shallow, muddy subtidal areas and few intertidal flats. These model results are quite unrealistic compared to real-world tidal systems such as the Wadden Sea or the Western Scheldt, where channels are predominantly sandy and both sand- and mudflats exist. In the remainder of this paper, we will put limited focus on these unrealistic scenarios. Erosion interaction allows mobilization of poorly erodible mud, especially around the threshold between the non-cohesive and cohesive regime. This leads to an increased E_{mud} with p_{mud} for mixtures with $p_{mud} \approx p_{mud,crit}$ (see also Figure 1b), whereas for higher p_{mud} the erodibility decreases. This allows transport of mud toward tidal flats, such that they become progressively more difficult to erode (as sedimentation of mud continues), enabling (large) mudflat formation and stabilization.

Simulations with high $\tau_{e,mud}$ and only roughness interaction do not develop a realistic morphology because the mud is not sufficiently mobile (as explained above). However, roughness interaction can promote mudflat growth when combined with more mobile mud. This effect is strongest for $\tau_e = 0.25$ Pa (as will also follow later from Figure 6c), where more and larger mudflats develop in the central parts of the basin when accounting for this
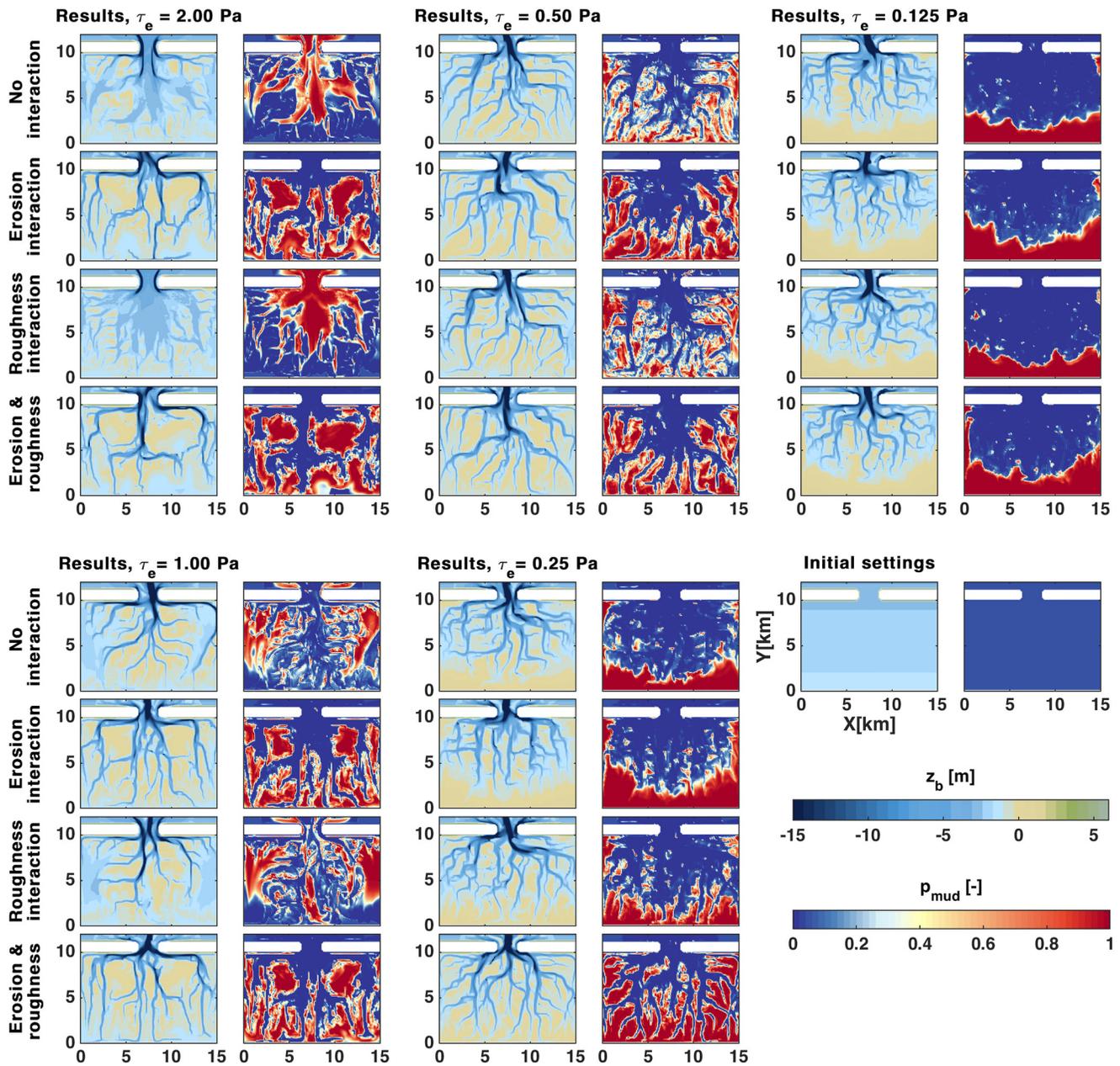
Figure 2. Modeled morphological evolution (50 years) of a synthetic tidal basin for a range of erosion settings, showing computed bed levels (z_b, left panel per model realization) and sediment composition (mud content, p_{mud}) of the upper bed (0.1 m, right panel).

effect (and even more when combined with erosion interaction). The physical explanation hereof is that when the bed shear stress is close to the critical bed shear stress for erosion, roughness interaction lowers the bed shear stress below the critical value. This reduction in erosion rates leads to increased net mud deposition, thereby further lowering the bed shear stress—a positive feedback mechanism leading to progressive mud deposition.

Not only the interaction method, but also the type of mud (in terms of erodibility) largely influences the morphodynamic evolution. In general we observe that large intertidal shoals are formed in the central parts of the basin when applying a high τ_e (1 or 2 Pa) in combination with erosion interaction. Herein we define intertidal shoals as intertidal flats that are surrounded by channels. Intertidal flats adjacent to the outer contours of the basin are referred to as fringing flats. With medium high τ_e (0.5 Pa), muddy shoal formation occurs at all scenarios. For more easily erodible mud ($\tau_e = 0.25$ Pa), especially fringing mudflats develop while the shoal size decreases. With $\tau_e = 0.125$ Pa, only fringing mudflats can develop.
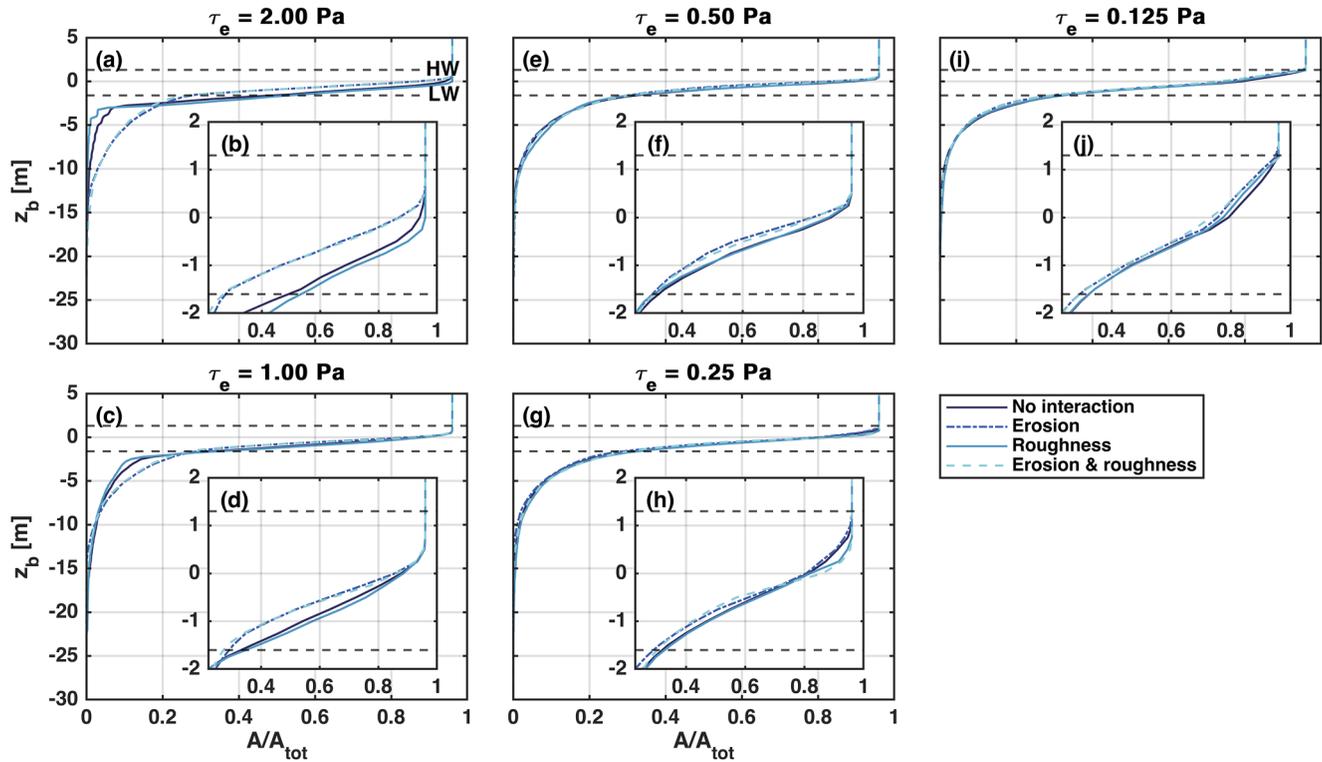
Figure 3. Hypsometric curves showing the cumulative area (A) per bed level (z_b), organized per τ_e. The black dashed lines mark the low water (LW) and high water (HW) lines. Inset plots zoom in on the intertidal areas.

In the following sections, we will evaluate the numerical model results in a more quantitative and aggregated way by computing tidal basin hypsometry, the size and type of intertidal area, and characteristics of the subtidal areas.

4.2. Hypsometry

Figures 3 and 4 show the computed hypsometric curves after 50 years of evolution, organized per τ_e and per interaction type respectively. These hypsometric curves are interpreted in terms of changes in intertidal area (between high and low water) and subtidal area (with the space between low water and −5 m representing the higher subtidal, and deeper water the lower subtidal).

Low mud erodibility without erosion interaction largely increases the subtidal area, at the expense of the lower/mid intertidal area (up to $z_b = 0.5$ m; Figures 3a, 3b, and 4a–4d). With erosion interaction, the intertidal area is similarly large for all models regardless of the choice for τ_e (Figure 4f). However, the spatial patterns do differ strongly (e.g., less but larger intertidal flats for high τ_e, see Figure 2). Conversely, without erosion interaction (Figures 4a–4d), the hypsometry strongly depends on τ_e. Our idealized tidal basin only developed higher intertidal area ($z_b > 0.5$ m) for very low τ_e. The limited development of the higher intertidal area is probably a result of the sheltered environment with limited waves along the borders of the basin, the absence of extreme storms and surges and the oversimplification of the tidal signal (de Vet et al., 2018; Galiforni-Silva et al., 2020; Schrijvershof et al., 2023).

The individual hypsometries are aggregated by averaging per model scenario (see Figure 5), showing that in general, erosion interaction leads to expansion of the intertidal area at the cost of the higher subtidal areas becoming deeper. The more mobile the mud, the higher the intertidal bed levels. However, the total size of the intertidal area remains approximately the same, except for the extreme case of $\tau_e = 2$ Pa.

4.3. Development of Intertidal Areas

4.3.1. Total Intertidal Area

The hypsometric curves after 50 years are subsequently aggregated into areas of sandy, muddy and total intertidal area (Figure 6). The total intertidal area A_i reveals that within the range 0.125 Pa $\leq \tau_e \leq$ 0.5 Pa, A_i depends little
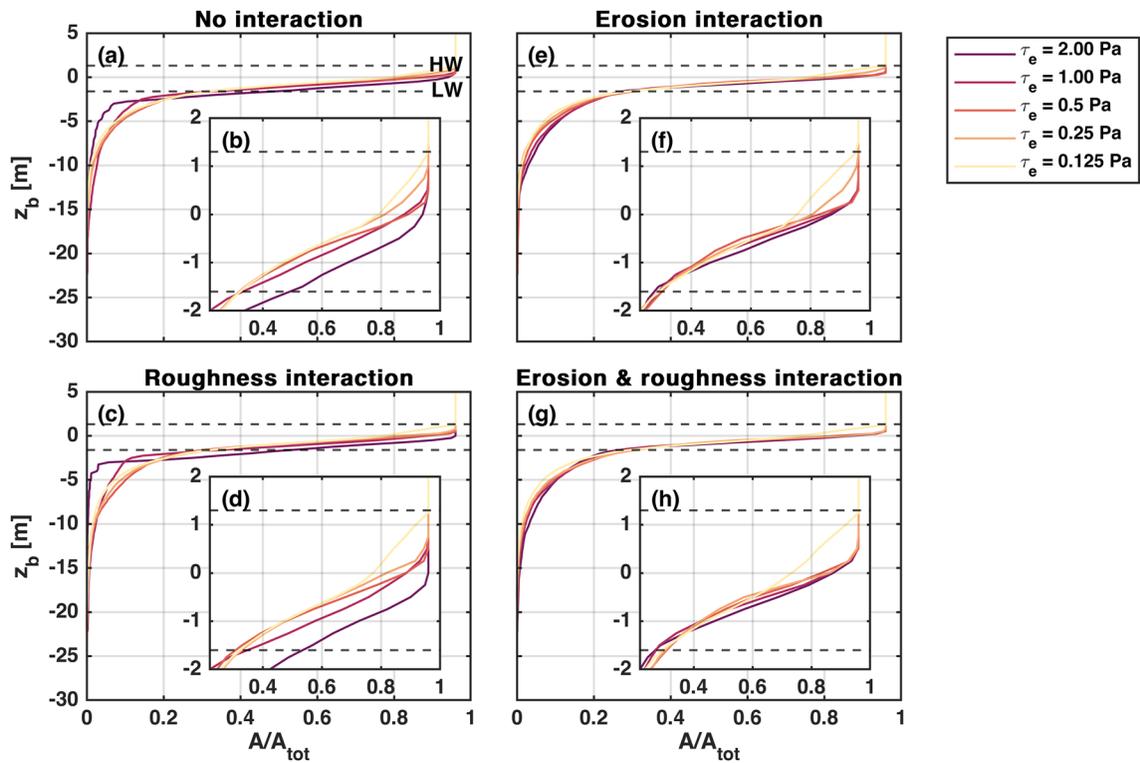
Figure 4. Hypsometric curves showing the cumulative area (A) per bed level (z_b), organized per interaction type. The black dashed lines mark the low water and high water lines. Inset plots zoom in on the intertidal areas.

on the type of sand-mud interaction, and varies between 63% and 67% (95–100 km^2). For $\tau_e > 0.5$ Pa, erosion interaction leads to an increase of the intertidal area of up to 5% compared to scenarios with $\tau_e \leq 0.5$ Pa. The rapid decrease in A_i at higher τ_e when not accounting for this type of interaction is considered unrealistic (as discussed earlier).

4.3.2. Sediment Composition

We further analyze intertidal flat dynamics by defining non-cohesive beds ($p_{mud} < 0.3$, Figure 6b) as sandy intertidal areas ($A_{i,sand}$) and cohesive beds ($p_{mud} \geq 0.3$, Figure 6c) as muddy intertidal areas ($A_{i,mud}$). Scenarios with erosion interaction strongly differ from simulations without erosion interaction, whereas simulations with
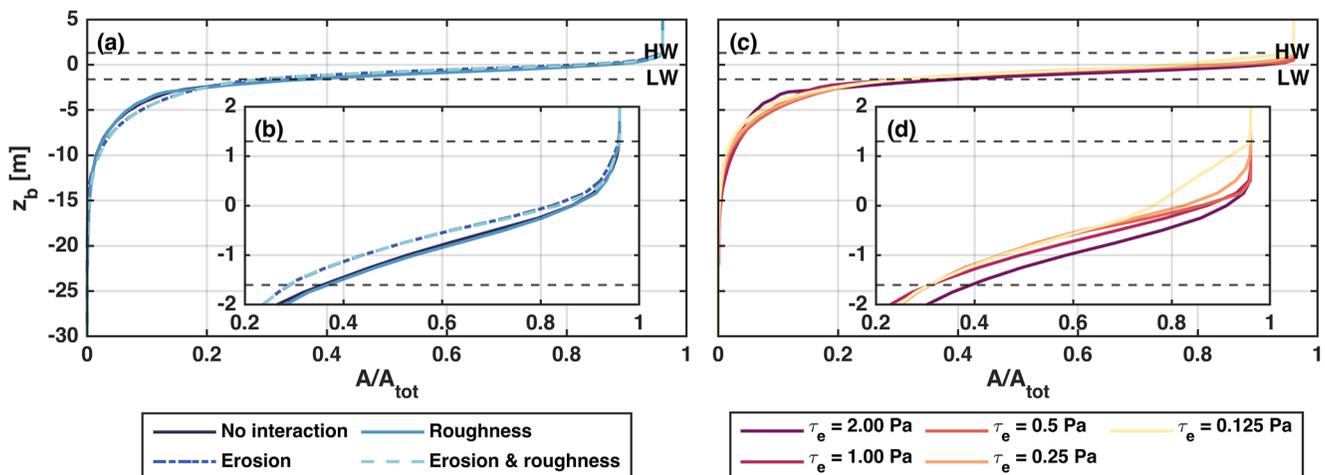

Figure 5. Combined hypsometric curves of averaged results. The black dashed lines mark the low water and high water lines. Inset plots zoom in on the intertidal areas.
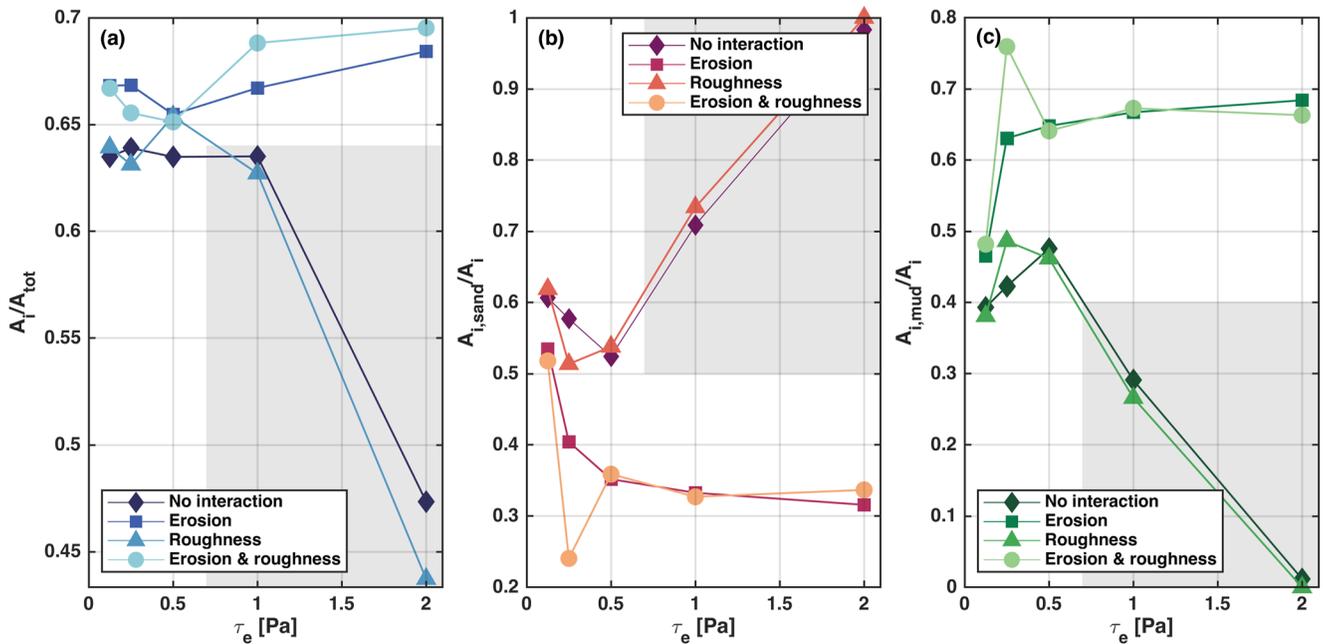
Figure 6. Development of intertidal areas. (a) Total intertidal area relative to the total basin area (150 km²), A_i/A_{tot}. (b) Relative sandy intertidal area $A_{i,sand}/A_i$. $A_{i,sand}$ is defined as the intertidal area with a non-cohesive sediment composition (i.e., $p_{mud} < 0.3$). (c) Relative muddy intertidal area $A_{i,mud}/A_i$. $A_{i,mud}$ is defined as the intertidal area with a cohesive sediment composition (i.e., $p_{mud} \geq 0.3$). The gray boxes represent a model parameter space yielding unrealistic results which are excluded from further analysis.

roughness interaction only slightly deviate from simulations without it. In general we observe a decreasing trend of $A_{i,sand}$ and an increasing trend of $A_{i,mud}$ with increasing τ_e for simulations with erosion interaction.

Without sand-mud interaction, $A_{i,mud}$ is highest (and $A_{i,sand}$ lowest) at $\tau_e = 0.5$ Pa. Mud with high τ_e is too immobile to reach the flats and remains in the channels, which results in unrealistic results. With erosion interaction, in the non-cohesive regime mud erosion increases with increasing p_{mud} (see also Figure 1b) until $p_{mud,crit}$, after which it decreases. This allows for mud to be eroded from the (sandy) channels (regardless of the very high τ_e) and be transported toward the flats, where mud accumulates and therefore erosion rates decrease again. This mechanism thus enables modeling of large mudflat formation during low-energy tide-dominated conditions as well as stabilization, allowing the flats to survive episodic storms. The effect of roughness interaction on morphology is much more subtle than that of erosion interaction. Roughness interaction enhances mudflat formation for relatively mobile mud ($\tau_e = 0.25$ Pa), which was already indicated by Figure 2.

Interestingly, the absolute maximum predicted values for $A_{i,sand}$ and $A_{i,mud}$ are fairly similar (around 60–70 km²), but require very different model settings. Moreover, the variability of $A_{i,sand}$ and $A_{i,mud}$ over the various scenarios is much larger than the variability of the total intertidal area A_i. The sediment composition is thus much more sensitive to the model settings related to sand-mud interaction than the total intertidal flat area. Despite a fairly constant total intertidal area, the size of individual shoals does strongly differ among the various scenarios, as will be explored hereafter.

4.3.3. Intertidal Flat Size

The analyzed model parameter space results in a striking variation in flat size. We analyze the flat size by calculating the exceedance probability of the distance from the subtidal areas of all grid cells with $z_b >$ low water (LW) (i.e., the intertidal areas, see Figure 7). This is similar to Edmonds et al. (2011)'s calculation of the nearest-edge distance of shoals in river deltas. An overall large probability reflects small intertidal flats and vice versa. To prevent confusion, we have left out the unrealistic results of the models with $\tau_e \geq 1.0$ Pa and without erosion interaction.

The remaining simulations with $\tau_e \geq 1.0$ Pa result in the formation of relatively large shoals (see also Figure 2). The shoal size is smallest for $\tau_e = 0.5$ Pa (comparing Figures 7a–7c) but it increases again at lower τ_e (Figures 7d
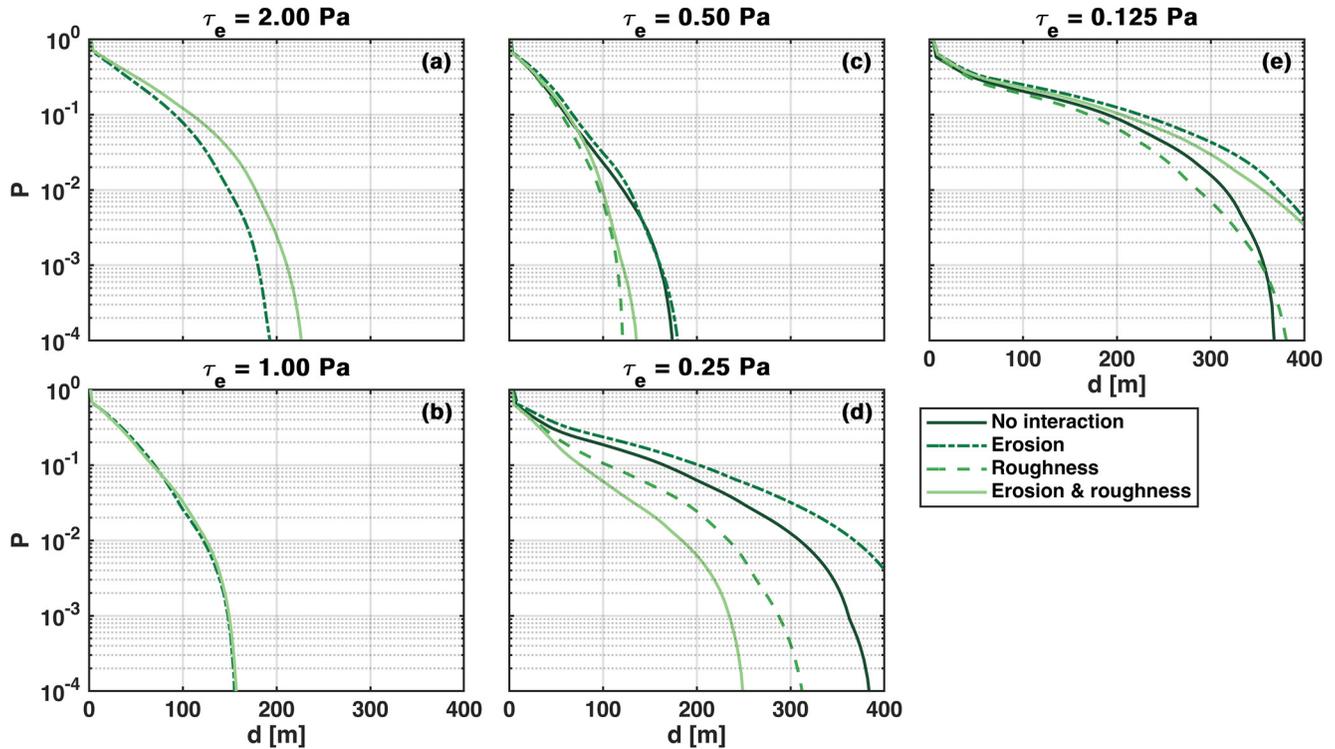
Figure 7. Probability of exceedance (P) of minimum distance to channel (d).

and 7e). This increase at low τ_e is caused by progressive growth of fringing flats bordering the basin boundaries with large distances to the channels, outpacing the decline of shoals in the central basin. The size of these fringing flats increases with decreasing τ_e. In general we observe the largest distances from the flats to the channels for erosion interaction only; roughness interaction reduces the development of fringing flats.

4.4. Development of Subtidal Areas

4.4.1. Areas and Volumes

To quantify the effect of sand-mud interaction and model parameter settings on the development of subtidal areas, we have determined the total relative subtidal area (A_s/A_{tot}) and absolute volume (V_s) for the deep subtidal (depth $d > 5$ m, $A_{s,deep}$, $V_{s,deep}$) and for the shallow subtidal ($d \leq 5$ m, $A_{s,shallow}$, $V_{s,shallow}$, see Figure 8). Again, we have marked unrealistic scenarios (yielding the largest variation) with gray boxes and exclude them from our analyses. A_s (Figure 8a) is relatively stable regardless of τ_e and shows a variability of <5% resulting from the type of sand-mud interaction. On the other hand, V_s (Figure 8d) shows a larger variability (35%), mainly because of the variation of τ_e and much less depending on the sand-mud interaction method.

$A_{s,shallow}$ decreases with increasing τ_e (Figure 8c) whereas $A_{s,deep}$ (Figure 8b) increases with increasing τ_e. The trend in $A_{s,shallow}$ corresponds to that of the total subtidal area A_s because about 70% of the subtidal area is shallow. Despite of its limited contribution to the area, the deep subtidal contributes to 60%–80% of the total channel volume and therefore the trends of $V_{s,deep}$ largely follow the trends of $V_{s,total}$. Here, we observe that an increase in τ_e leads to an increase in $V_{s,deep}$ and a decrease in $V_{s,shallow}$ (within the considered range of τ_e).

4.4.2. Channel Depth

The channel depth is further analyzed by visualizing the distribution of the bed level occurrence in the deeper subtidal (Figure 9). The maximum channel depth varies between 17.5 and 23 m, whereas the median depth (white dots) is very stable (around 7 m). The mean depth, marked with the black lines, is slightly larger (around 8 m). These values are not directly correlated with τ_e nor with the types of sand-mud interaction.

Scenarios with a higher τ_e do not necessarily lead to more overall erosion or deeper channels: for all model scenarios the median bed level of the deeper subtidal areas varies between −7 and −8 m only. Since channels are,
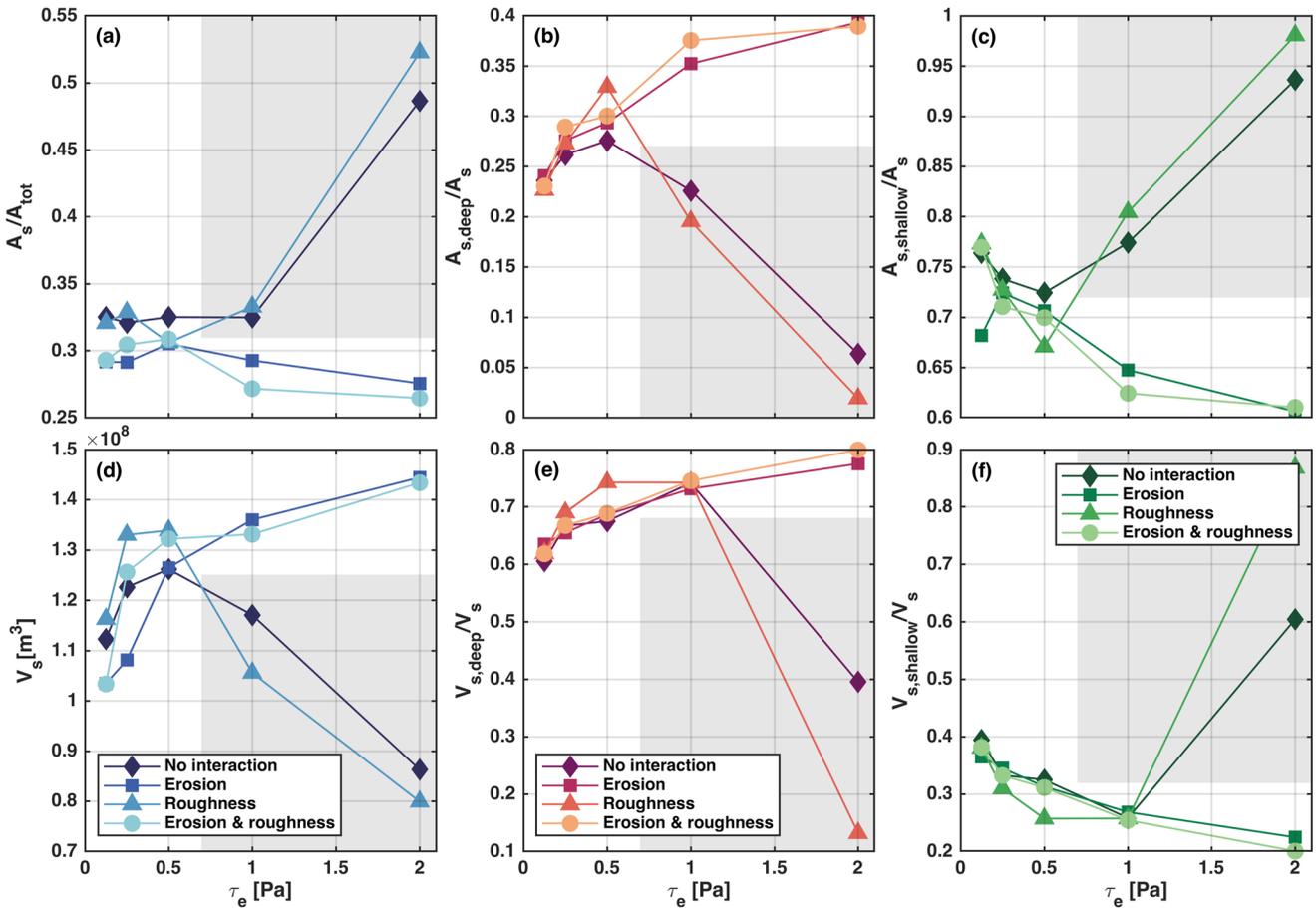
Figure 8. Development of subtidal area and volumes. (a) Total subtidal area A_s relative to the total basin area (A_{tot}, 150 km^2). (b) Relative deep subtidal area $A_{s,deep}$/A_s, defined as the subtidal areas below −5 m. (c) Relative shallow subtidal area $A_{s,shallow}$/A_s, defined as the subtidal area between low water and −5 m. (d–f) Subtidal volumes $V_{s,total}$, $V_{s,deep}$, $V_{s,shallow}$. The gray boxes represent a model parameter space yielding unrealistic results which are excluded from further analysis.
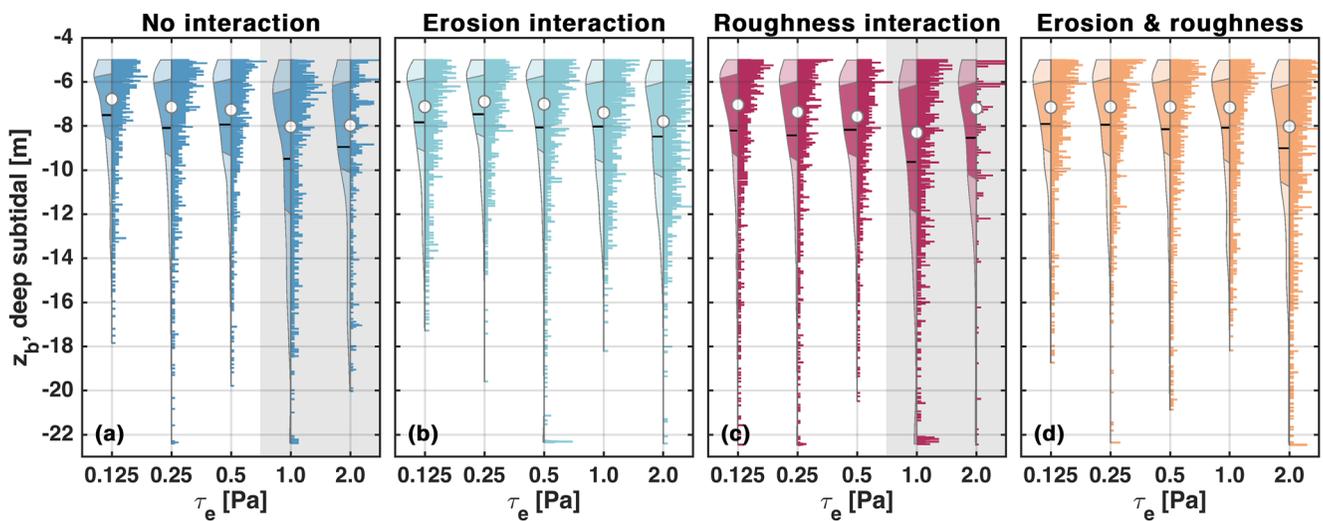

Figure 9. Channel depth variation: violin plots (including histograms right of the violin plot) show the bed level (z_b) occurrence in the deeper subtidal areas. Violin plots are a combination of a kernel density plot and a box plot, providing the distribution of the data as well as a summary of its statistics. The white dots show the median values, the black bars indicate the mean values. The interquartile range (between 25% and 75%) is displayed with a shadow. The histograms right of the plots show the distribution over the depths at a greater detail. The gray boxes represent a model parameter space yielding unrealistic results which are excluded from further analysis.
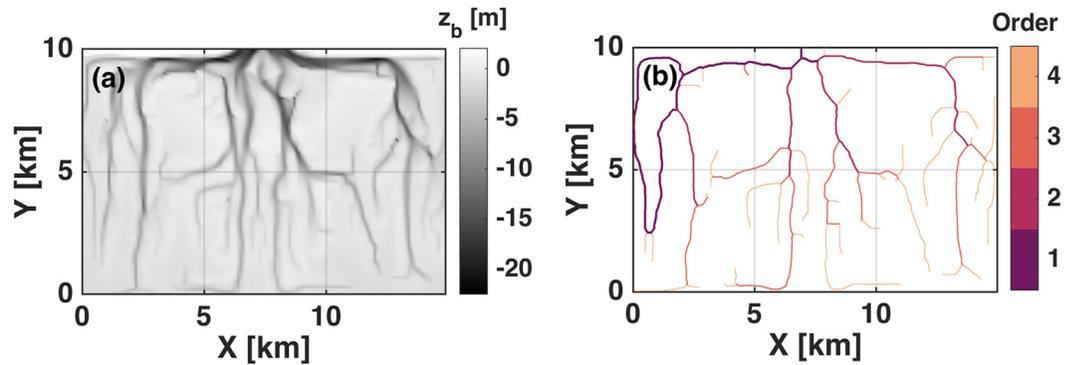
Figure 10. (a) Digital elevation model (bed levels z_b), derived from Delft3D output. (b) Extracted channel structure and computed reverse Strahler order.

both in our models and in reality, predominantly sandy, erosion rates will mainly be determined by sand characteristics. This explains the small differences between the various model scenarios and the minor dependence on the investigated parameter settings. Factors that are more likely to affect channel depths are hydrodynamic forcing and sand grain size.

4.4.3. Channel Length and Complexity

To further analyze the channel patterns, we make use of Chirol et al. (2018)'s creek parametrization algorithm by extracting the channel data below low water. This enables a morphometric analysis of the dimensions and complexity, including the reverse Strahler order. The Strahler order is a numerical measure of the branching complexity. In the Strahler method, all links without any tributaries are assigned an order of 1 and are referred to as first order. When channels of the same order intersect, the order increases. Intersection of two channels of different orders does not result in an increase in order. Following Chirol et al. (2018, 2022), we convert the Strahler order to a reverse Strahler order (see Figure 10). The benefit of using reverse Strahler ordering compared to traditional Strahler ordering is that reverse Strahler ordering ensures that the entry channel at the basin inlet is always classified as the first order.

The total channel length in the basin (L_{tot}) is obtained by summation of the length of all individual channels (Figure 11a). A high L_{tot} may result from for example, many short channels (complex system), less but longer channels (less complex system), or a high sinuosity. For all model scenarios L_{tot} increases with τ_e up to $\tau_e = 0.5$ Pa, because channels penetrate deeper into the basin at cost of the fringing flat development. Less channels develop for $\tau_e > 0.5$ Pa, and L_{tot} decreases with increasing τ_e.
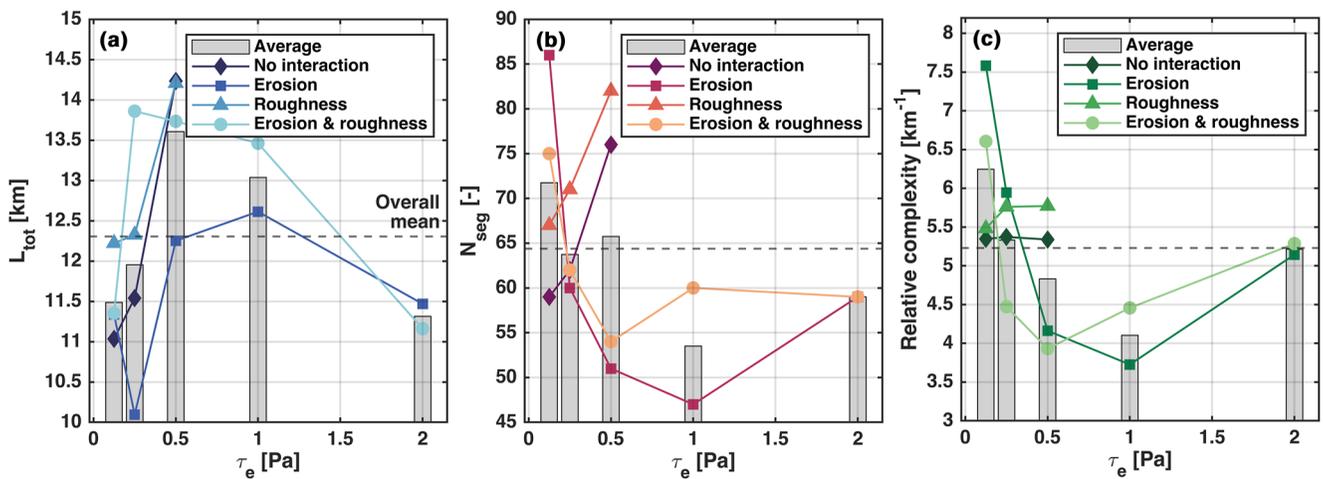
Figure 11. (a) Total channel length (sum of all channels in the model, L_{tot}) depending on τ_e and the interaction type. Scattered lines show the model results for all models except for scenarios 1, 3, 5, 7 (unrealistic). Histograms show the average per τ_e choice. Dashed line shows the overall mean value. (b) Total number of channel segments (N_{seg}) depending on τ_e and the interaction type. (c) Relative complexity, defined as the number of segments divided by the total channel length (N_{seg}/L_{tot}), depending on τ_e and the interaction type.

Figure 12. Violin plots including histograms showing the channel properties per reverse Strahler order. Values are based on the mean properties per scenario, showing the (a) va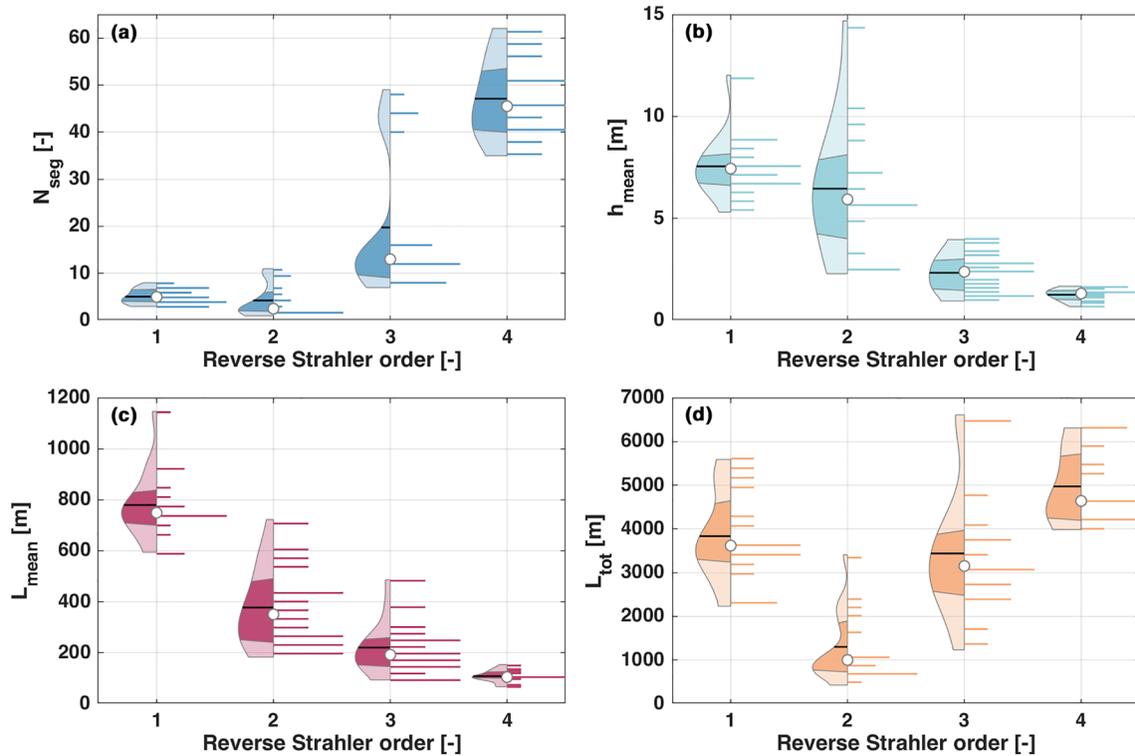riance of the average number of segments N_{seg}, (b) mean channel depth h_{mean}, (c) mean channel length L_{mean}, and (d) total channel length L_{tot} per reverse Strahler order.

The complexity of the channel patterns (Figure 11c) is defined as the number of channel segments (Figure 11b) divided by the total channel length (Figure 11a). A segment is defined as a channel part in between a bifurcation or confluence. With erosion interaction, both the number of segments and the relative complexity generally increase with decreasing τ_e. Without erosion interaction the number of segments decreases with decreasing τ_e and the relative complexity is independent of τ_e.

Channel complexity can be further analyzed by determining the reverse Strahler order of the channels (see also Figure 10). Figure 12 shows the occurrence of the number of segments, mean channel depth, mean channel length and total channel length of all model scenarios. Herein, we have first calculated the average values of these parameters per reverse Strahler order of each model scenario, such that Figure 12 shows the variability between model scenarios. As expected, the number of segments increase with reverse order increase, whereas the mean channel depth and length decrease. More interesting is that channel complexity (in terms of number of segments) is especially depending on scenarios for inverse Strahler order 3 and 4, while depth and length are more depending at lower inverse Strahler number. The total channel length is not clearly correlated with the Strahler number because it is influenced by both the number of segments and the segment length.

4.5. Comparison With Field Data

To determine the validity of our model results and identify what combination of parameters most closely resembles the morphology of actual tidal basins such as those in the Wadden Sea, we compare our model output to field data. Herein, we focus on those aspects and metrics that are most influenced by the investigated sand-mud interaction mechanisms, being the morphological evolution (Figure 2), the hypsometry, channel patterns, and intertidal area development (within the latter especially the sediment composition). We make use of recent bathymetry data from the *Vaklodingen* and *EasyGSH* data sets and sediment composition data from the *Sediment Atlas Wadden Sea*, *SIBES* and *EasyGSH*.

Figures 13a–13e show the bathymetries of five basins within the Dutch and the German Wadden Sea. We observe a relatively large morphologic variation in terms of bed levels and channel patterns, which may at least partly
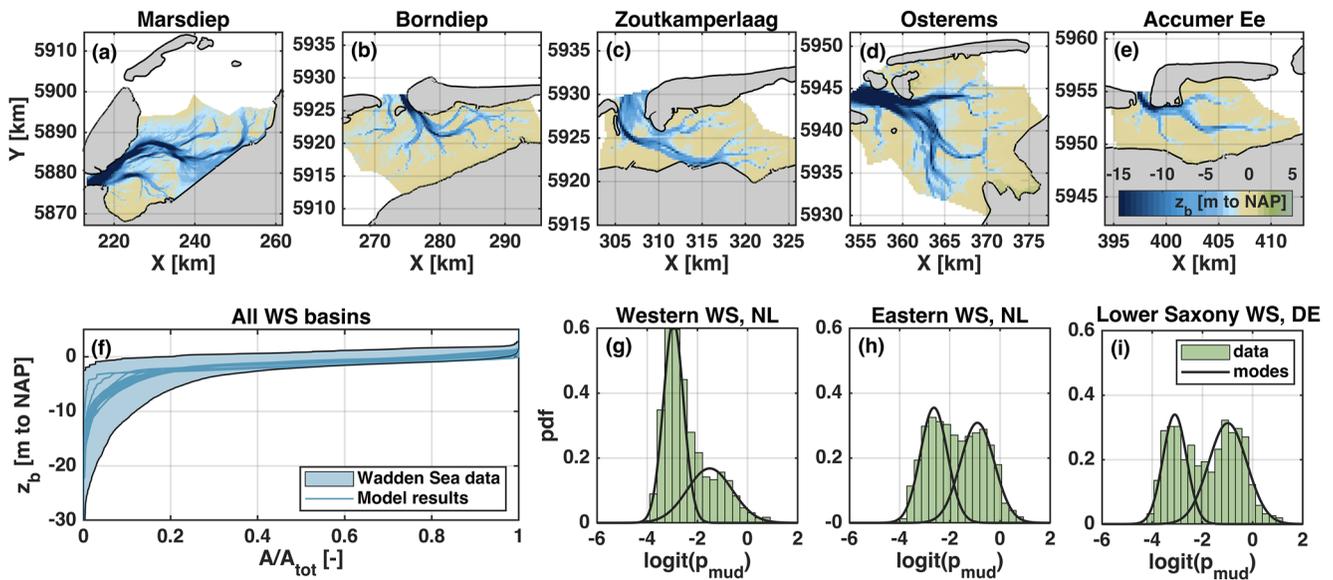
Figure 13. Morphology of the Wadden Sea (WS) basins. (a–e) Bed levels of five basins in the Dutch (*Vaklodingen* data) and German Wadden Sea (*EasyGSH* data), plotted in *m* to NAP (Dutch Ordnance Datum). (f) Envelope of the hypsometric curves of all Dutch and German basins, excluding the estuaries, compared to the modeled hypsometries. (g–i) Bimodal distribution p_{mud} of the upper sediment bed on the intertidal areas of the Wadden Sea basins, based on Colina Alonso et al. (2022).

be explained by the variation in basin size and shape. Figure 13f shows the range of hypsometries of all Dutch and German Wadden Sea basins (excluding the Ems, Weser and Elbe estuaries). This range is much larger than the variability that was obtained by varying sand-mud interaction settings and/or mud erodibility settings in our model (see the blue lines and also Figures 3 and 4). Cleveringa and Oost (1999) showed that the Wadden Sea basins contain similar characteristics as three- to four-times branching channel networks, with logarithmically decreasing branch lengths and increasing number of channels with increasing channel order. This is in line with our schematized model results (Figure 12). However, they also show that the total channel length largely varies per basin, showing a much greater variation than our model results. This large natural variability in channel patterns and bed levels, resulting from among others the tidal basin shape, makes it difficult to state whether including sand-mud interaction improves the model performance regarding hypsometry and channel type.

The sediment composition of the Wadden Sea flats varies both on the large-scale (e.g., the Eastern Dutch Wadden Sea is more muddy than the Western Dutch Wadden Sea) and on the small-scale (e.g., large changes in the mud content over several 100's of meters and the occurrence of isolated mud patches in sand dominated environments; Colina Alonso et al., 2021; de Glopper, 1967; Oost, 1995). The overall sediment composition of the intertidal flats can vary strongly depending on among others the geometry of the basin, the hydrodynamic forcing and the suspended sediment concentration. Figure 14 shows the intertidal area in the Wadden Sea basins A_i (relative to the total area of the basins) and the contribution of non-cohesive sandy flats and cohesive mudflats to A_i. This is plotted against the basins' distance from Den Helder, following the coastline from West to East, such that the first data point is the Marsdiep tidal basin in the Netherlands and the last data point represents Lister Tief basin bordered by the German island Sylt and the Danish island Rømø. Danish basins are not included in this analysis, because of insufficient availability of bathymetry and sediment composition field data. Comparing the field data of the Wadden Sea (Figure 14) with our model results (Figure 6) shows that our predicted total intertidal area is within the observed range (which is again much wider), although the predicted contribution of sandy flats compared to mudflats is generally on the low side and best resembles the East-Frisian Wadden Sea (basins 12–20).

An important characteristic of the mud content in the Wadden Sea (and probably also in other tidal basins) is its bimodal distribution: the bed tends to be relatively sandy or relatively muddy, with fewer observations in between (Colina Alonso et al., 2022). This bimodality is most clearly visible after logit-transformation and is most pronounced on the intertidal areas (see Figures 13g–13i). Although bimodality is observed in the entire Wadden Sea, the location of the second mode (showing how muddy the mudflats are) varies within the system, with for example, a larger mud content in the Eastern Wadden Sea compared to the Western Wadden Sea. Figure 15 shows the distribution of the mud content in the intertidal areas of our schematized model output. All models
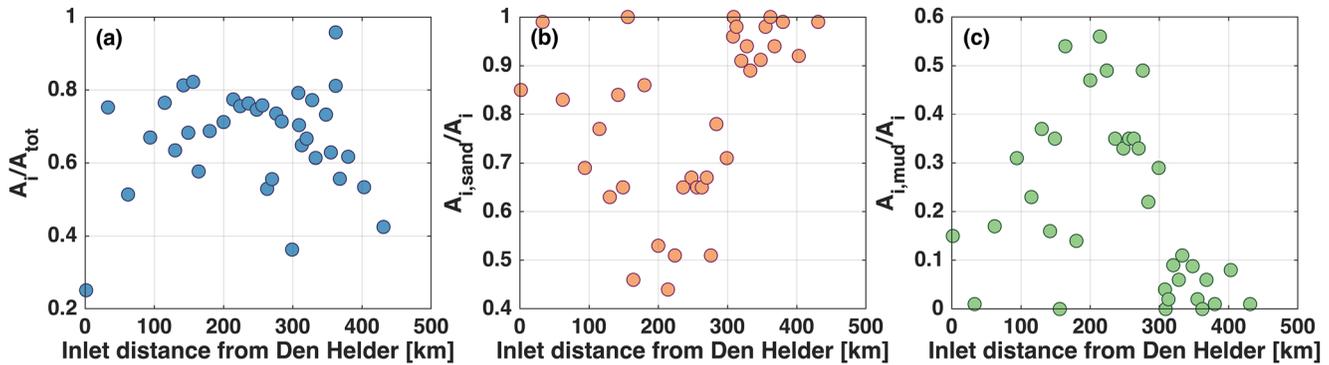
Figure 14. Intertidal areas in the Wadden Sea basins plotted against the distance of the basin inlet to Den Helder (starting West with the Marsdiep basin and moving East and North up-to Lister Tief basin). (a) Total intertidal area relative to the total basin area, A_i/A_{tot}. (b) Relative sandy intertidal area $A_{i,sand}/A_i$ (c) Relative muddy intertidal area $A_{i,mud}/A_i$. $A_{i,sand}$ and $A_{i,mud}$ are defined as in Figure 6.

without sand-mud interaction fail to reproduce this bimodality (marked in gray), either because the distribution is unimodal or because a bimodality is predicted with a second mode at $p_{mud} \approx 99\%$, which is unrealistically high in these systems. Models with erosion interaction and $\tau_e \geq 0.5$ Pa do reproduce the bimodality, even though they slightly underestimate the mud content in the sandy areas ($p_{mud,mode1} \approx 0.01$ whereas in reality this is approximately 0.04) and overestimate the mud content in the muddy areas ($p_{mud,mode4} \approx 0.50$ while in the Frisian Wadden Sea this is typically 0.35–0.40). In terms of the mud content within the bed, erosion interaction is therefore an important improvement.

5. Discussion

5.1. Using Schematized Models

Schematized model environments are an essential tool to improve our knowledge on morphodynamics. However, when the model conditions are strongly idealized, it becomes difficult to correlate such model findings with
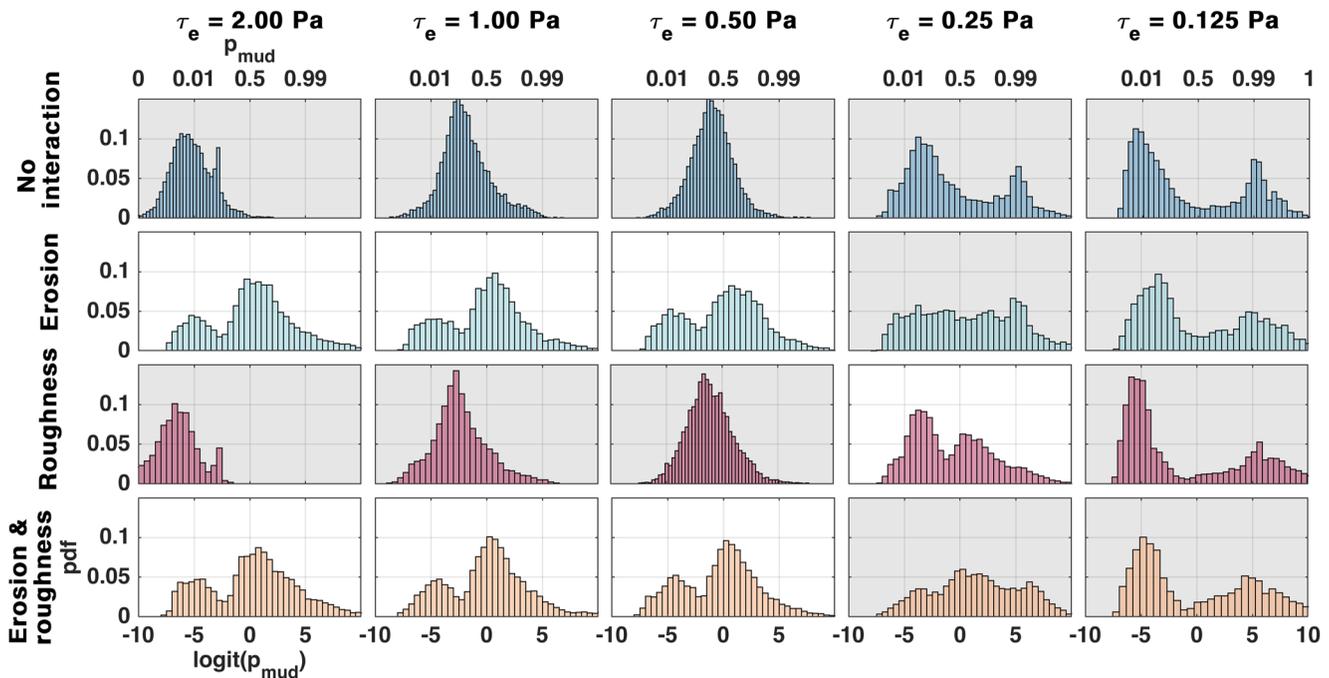

Figure 15. Distribution of the mud content, after logit-transformation, in the upper sediment bed of the numerical models. The upper y-axes show the corresponding p_{mud} values. The gray panels indicate the models that do not reproduce a realistic distribution, either because it is unimodal or because the second mode has a value ≥ 0.99.

processes that take place in reality. The main aim of this research was to better understand the effects of small-scale sand-mud interaction on the (modeled) morphodynamics of tidal basins. In order to reduce complexity and restrict the degrees of freedom (and thus number of simulations) we strongly schematized tidal basin geometry and boundary conditions. We have quantified the effects of sand-mud interaction by defining a number of morphologic metrics, but we also observe that some of these metrics vary even more in reality due to for instance the large-scale variability in tidal prism, storminess or suspended mud concentrations (Zhou et al., 2021, 2022) and the basin geometry on a smaller scale (e.g., comparing adjacent Wadden Sea basins; Cleveringa & Oost, 1999; Ridderinkhof et al., 2014). And even though our model simulations fit within the range of morphological metrics that describe the basins in the Wadden Sea, they are most useful to analyze in comparison with each other.

5.2. Effects of Sand-Mud Interaction on Morphodynamic Evolution

Including sand-mud interaction in modeling studies provides a better representation of underlying physical processes. Our model results show that sand-mud interactions impact long-term basin evolution: The patterns and intertidal flat shape, size and composition vary with mud erodibility settings, but equally with the considered sand-mud interaction method. We have demonstrated that sand-mud interactions steer large-scale morphodynamic evolution by enhancing intertidal flat formation, with erosion interaction having a much larger effect than roughness interaction—which is strongest for scenarios with poorly erodible mud ($\tau_e > 1$ Pa). Roughness interaction also enhances mudflat formation, but for a narrower range of conditions: our results show that this interaction type is mainly effective when mud is still relatively mobile ($\tau_e = 0.25$ Pa). We believe that this condition may however be different in other systems with different forcing, since we expect roughness interaction to have the largest effect when the bed shear stresses are close to the critical bed shear stress for erosion.

Yet, most effects of including sand-mud interaction on the morphologic metrics are more subtle than the observed natural variability in the field. An exception is the bimodal distribution of the mud content, which is observed in the Wadden Sea basins, but cannot be reproduced by our numerical models when omitting sand-mud interaction. But even though sand-mud interaction mechanisms improve the morphodynamic simulations, the underlying formulations still need to be more vigorously validated. Sand-mud erosion formulations, such as those by van Ledden (2003) but also others (e.g., Bi & Toorman, 2015; D. Chen et al., 2021; Jacobs et al., 2011; Le Hir et al., 2011; Mengual et al., 2017; van Rijn, 2020), have only been verified for a limited range of conditions. Erosion rates predicted by these formulations should be compared to more extensive laboratory experiments in controlled environments. We especially recommend to execute more erosion experiments of sand-mud mixtures under combined forcing of currents and waves, which are only limitedly available at this moment, to improve our understanding of sand-mud dynamics.

Additional advances related to the physical behavior of sand-mud beds that should preferably be incorporated in sand-mud models are the dynamic behavior of bed forms and the role of biology in flocculation. Baas et al. (2021) have presented a new bedform phase diagram of current- and wave-generated bedforms in mixed sand-mud tidal environments. The presence of small amounts of clay can significantly reduce the bedform size (Baas et al., 2013), but also the steepness (Schindler et al., 2015). We have performed a first assessment of the effects of the imposed total drag because of different bedform sizes (see Supporting Information S1). Here, we have compared the models with a total drag corresponding to bedforms in sandy systems ($k_{s,hydro} = 0.02$ m, see Table 1), to models with (bedform-related) roughness heights that are 5 and 10 times smaller. The results show that, even though the bedform-related roughness does influence the hydrodynamics, its effect on the morphodynamic development remains limited in comparison with the investigated sand-mud interaction mechanisms (see Figures S2 and S3 in Supporting Information S1). Note that herein, we do not account for varying bedform dimensions depending on the bed sediment composition, which can introduce second order effects. Manning et al. (2011) showed that because of the greater binding effect of biology, sand particles can also flocculate with mud. This flocculation interaction may therefore result in joint transport of sand and mud. Spearman et al. (2011) demonstrated that including flocculation interaction into sand-mud models improves reproduction of the observed sediment dynamics. We recommend to include these additional sand-mud interaction mechanisms and evaluate their impact on long-term morphodynamic predictions by developing model scenarios which become progressively more complex, starting from simulations without sand-mud interaction mechanisms.

5.3. Modeling Guidelines for a Phenomenological Optimization

Relating sand-mud interaction mechanisms to aggregated morphological metrics, such as the intertidal area or the channel pattern complexity, leads to an improved process understanding of the morphological consequences of

these mechanisms. Consequently, it also allows a phenomenological optimization of morphodynamic models on a high aggregation level. Since we have identified how channels and shoal patterns vary with sand-mud parameters, these parameters can be used to optimize schematized models toward real-life systems. We may therefore translate our sensitivity analysis on sand-mud processes and settings into a methodology to improve morphological model metrics, resulting in the following guidelines:

- **Intertidal area**: The overall intertidal area slightly increases by including erosion interaction. Promoting the development of higher intertidal areas requires inclusion of a mud fraction with low erodibility.
- **Shoal size**: Large (non-fringing) muddy intertidal shoals develop when sediment is poorly erodible (i.e., applying a high critical shear stress for mud) combined with erosion interaction. Large fringing flats and smaller intertidal shoals develop when the critical bed shear stress is lower.
- **Shoal composition**: Including erosion interaction generally leads to a higher mud content in the intertidal areas. The impact of erosion interaction on mud content becomes larger with increasing critical bed shear stress for mud erosion. In order to model large mudflat formation within our parameter settings, we thus advise to include erosion interaction and poorly erodible mud (a τ_e of 1–2 Pa). When combined with erosion interaction, including roughness interaction generally leads to an additional increase in mud content (given that $\tau_e < 2$ Pa). Note however, that other parameter choices (e.g., suspended mud concentrations) will also affect the simulated shoal composition.
- **Subtidal area development:** The value of the critical bed shear stress has a stronger influence on the development of subtidal areas and volumes than the type of sand-mud interaction mechanism included in the model. The total deep ($z_b < -5$ m) subtidal area and its total volume increases with increasing τ_e (within the considered range). Shallow intertidal areas (-5 m $< z_b \leq$ LW) show an opposite trend.
- **Channel pattern complexity:** Channel complexity—defined as the number of channels corrected for the total channel length—increases for lower critical bed shear stress for mud erosion. This will however only have an effect on model results when erosion interaction is included in the model, since simulations without erosion interaction show very little variation in the complexity (regardless of the value of τ_e).

Using the method of Soulsby and Clarke (2005) to calculate bed shear stresses under flow and wave forcing in morphological models has an important additional benefit, next to those obtained by including roughness interaction. Hydrodynamic models are commonly calibrated by modifying the bed roughness parameter (e.g., including spatially varying roughness fields, reflecting bedforms or subgrid bathymetric effects). The resulting bed roughness is subsequently also used for sediment transport computations through its impact on the bed shear stress. This may result in realistic hydrodynamic results, but introduces inconsistencies when modeling morphodynamics. Preferentially, the bed roughness used for morphological modeling should therefore differ from the one used for calibrating the hydrodynamics. The formulations by Soulsby and Clarke (2005) provide such a decoupled bed roughness methodology.

5.4. Parametrization of Model Results for Comparison With Real-Life Systems

As explained in the introduction, schematized models are often used in studies related to the long-term morphodynamic behavior of deltas, for example, to determine their response to SLR. An important drawback of such schematized configurations is that the model results are difficult to compare with real-world systems. To improve the applicability of schematized models for real-life predictions, we therefore advocate the use of model validation metrics. Computing such metrics for both real-world systems and for the outcomes of highly schematized models allows a quantitative comparison of the model with real systems on a higher aggregation level.

We have synthesized our model results in a number of parameters that represent the shoal and channel properties in terms of geometry and topography, including the sediment composition. These metrics mainly focus on the aggregated meso-scale configuration of the system. For a more exhaustive real-life comparison, we recommend an extension of this parametrization with metrics that represent the large-scale configuration, such as those presented by Edmonds et al. (2011) and Broaddus et al. (2022), and by metrics that further analyze a system's complexity and dynamics, such as those presented by Tejedor et al. (2015). The latter introduce several parameters to determine delta's complexity in terms of topology (imposed by the network connectivity) and dynamics (introduced by the flux partitioning in the system). Their results reveal an inverse relationship between the vulnerability of a system and its complexity, showing the importance of the ability to simulate systems with similar complexity as real systems when analyzing their resilience to for example, large-scale human interventions and SLR.

6. Conclusions

We have studied long-term tidal basin evolution including two physical sand-mud interaction mechanisms, namely erosion interaction and roughness interaction. Erosion interaction implies that sand and mud interact in the sediment matrix of the sediment bed, and hence their erosion is coupled. Depending on the sediment composition, a sand-mud mixture can be non-cohesive, in which erosion is defined by the sand skeleton, or cohesive, in which the mud matrix determines the erosive behavior of the mixture. Roughness interaction implies that the sediment composition affects the hydraulic roughness of the sediment bed and therefore also the near-bed turbulence and thus the bed shear stresses. Consequently, an increase in the mud content of the bed lowers the bed shear stresses and thus weakens erosion forces.

Our results show that sand-mud interaction impacts tidal basin evolution, with erosion interaction having a much larger effect than roughness interaction. Especially the intertidal flat shape, size and composition widely vary with mud erodibility settings, but equally with the considered sand-mud interactions. Both interactions can enhance mudflat formation, though under very different circumstances: erosion interaction has a stronger effect in scenarios with poorly erodible mud ($\tau_e > 1$ Pa), whereas roughness interaction shows this effect in scenarios with high mud erodibility ($\tau_e = 0.25$ Pa). On the other hand, the effects of including sand-mud interaction on the overall hypsometry and channel depths remain limited, despite the very different erosion formulations applied.

Including sand-mud interaction in morphodynamic models provides a better representation of the physical processes. Sand-mud interaction may additionally (or consequentially), be used to optimize the morphodynamic model evolution. We show that in order to reproduce the bimodal distribution of the mud content, which is a typical characteristic of the bed composition in the Wadden Sea, one must account for sand-mud interaction. We have provided guidelines to improve schematized model evolution to resemble real-life systems through aggregated morphological metrics. When applying schematized model configurations, one of the main challenges is to translate model-based conclusions to the real world. We strongly advocate the use of morphological validation metrics—representing the shoal and channel properties in terms of geometry and topography, such as the ones that we have presented—as part of future work.

Data Availability Statement

There are no restrictions on the data used in this study. Input and output files of the numerical simulations are available at the 4TU.ResearchData repository (Colina Alonso et al., 2023): https://doi.org/10.4121/21431427. Bathymetry data of the Dutch Wadden Sea (*Vaklodingen*) is publicly available and can be requested through the servicedesk data of Rijkswaterstaat (2023): https://www.rijkswaterstaat.nl/formulieren/contactformulier-servicedesk-data. Bathymetry data of the German Wadden Sea (*EasyGSH*) are available at (Bundesanstalt Für Wasserbau, 2020): https://doi.org/10.48437/02.2020.K2.7000.0002. Sediment composition information was obtained from Colina Alonso et al. (2022), which used the *SIBES* data set, the *Sediment Atlas Wadden Sea* (Rijkswaterstaat, 1998), and via the *EasyGSH* data set (Sievers et al., 2020): https://doi.org/10.48437/02.2020.K2.7000.0005.

References

Baas, J. H., Davies, A. G., & Malarkey, J. (2013). Bedform development in mixed sand-mud: The contrasting role of cohesive forces in flow and bed. *Geomorphology*, *182*, 19–32. https://doi.org/10.1016/j.geomorph.2012.10.025

Baas, J. H., Malarkey, J., Lichtman, I. D., Amoudry, l. O., Thorne, P. D., Hope, j. A., et al. (2021). Current- and wave-generated bedforms on mixed sand–clay intertidal flats: A new bedform phase diagram and implications for bed roughness and preservation potential. *Frontiers in Earth Science*, *9*, 1–27. https://doi.org/10.3389/feart.2021.747567

Bi, Q., & Toorman, E. A. (2015). Mixed-sediment transport modelling in Scheldt estuary with a physics-based bottom friction law. *Ocean Dynamics*, *65*(4), 555–587. https://doi.org/10.1007/s10236-015-0816-z

Braat, L., van Kessel, T., Leuven, J. R. F. W., & Kleinhans, M. G. (2017). Effects of mud supply on large-scale estuary morphology and development over centuries to millennia. *Earth Surface Dynamics*, *5*(4), 617–652. https://doi.org/10.5194/esurf-5-617-2017

Broaddus, C. M., Vulis, L. M., Nienhuis, J. H., Tejedor, A., Brown, J., Foufoula-Georgiou, E., & Edmonds, D. A. (2022). First-order river delta morphology is explained by the sediment flux balance from rivers, waves, and tides. *Geophysical Research Letters*, *49*(22), e2022GL100355. https://doi.org/10.1029/2022GL100355

Brückner, M. Z. M., Schwarz, C., Coco, G., Baar, A., Boechat Albernaz, M., & Kleinhans, M. G. (2021). Benthic species as mud patrol-modelled effects of bioturbators and biofilms on large-scale estuarine mud and morphology. *Earth Surface Processes and Landforms*, *46*(6), 1–17. https://doi.org/10.1002/esp.5080

Bundesanstalt Für Wasserbau. (2020). EasyGSH-DB: Bathymetrie (1996–2016). [Dataset]. European Commission. https://doi.org/10.48437/02.2020.K2.7000.0002

Caldwell, R. L., & Edmonds, D. A. (2014). The effects of sediment properties on deltaic processes and morphologies: A numerical modeling study. *Journal of Geophysical Research: Earth Surface*, *119*(5), 961–982. https://doi.org/10.1002/2013JF002965

Chen, D., Zheng, J., Zhang, C., Guan, D., Li, Y., & Wang, Y. (2021). Critical shear stress for erosion of sand-mud mixtures and pure mud. *Frontiers in Marine Science*, *8*, 713039. https://doi.org/10.3389/fmars.2021.713039

Chen, X., Zhang, C., Townend, I. H., Paterson, D. M., Gong, Z., Jiang, Q., et al. (2021). Biological cohesion as the architect of bed movement under wave action. *Geophysical Research Letters*, *48*(5), 1–9. https://doi.org/10.1029/2020GL092137

Chirol, C., Haigh, I. D., Pontee, N., Thompson, C. E., & Gallop, S. L. (2018). Parametrizing tidal creek morphology in mature saltmarshes using semi-automated extraction from lidar. *Remote Sensing of Environment*, *209*, 291–311. https://doi.org/10.1016/j.rse.2017.11.012

Chirol, C., Haigh, I. D., Pontee, N., Thompson, C. E. L., & Gallop, S. L. (2022). Morphological evolution of creek networks in 10 restored coastal wetlands in the UK. *Scientific Data*, *9*(1), 1–16. https://doi.org/10.1038/s41597-022-01199-4

Cleveringa, J., & Oost, A. P. (1999). The fractal geometry of tidal-channel systems in the Dutch Wadden Sea. *Geologie en Mijnbouw/Netherlands Journal of Geosciences*, *78*(1), 21–30. https://doi.org/10.1023/A:1003779015372

Colina Alonso, A., van Maren, D. S., Herman, P. M. J., van Weerdenburg, R. J. A., Huismans, Y., Holthuijsen, S. J., et al. (2022). The existence and origin of multiple equilibria in sand-mud sediment beds. *Geophysical Research Letters*, *49*(22), e2022GL101141. https://doi.org/10.1029/2022GL101141

Colina Alonso, A., van Maren, D. S., Elias, E. P. L., Holthuijsen, S. J., & Wang, Z. B. (2021). The contribution of sand and mud to infilling of tidal basins in response to a closure dam. *Marine Geology*, *439*, 106544. https://doi.org/10.1016/j.margeo.2021.106544

Colina Alonso, A., van Maren, D. S., van Weerdenburg, R. J. A., Huismans, Y., & Wang, Z. B. (2023). Dataset accompanying the publication: Morphodynamic modeling of tidal basins: The role of sand-mud interaction [Dataset]. 4TU.ResearchData. https://doi.org/10.4121/21431427

Dastgheib, A., Roelvink, J. A., & Wang, Z. B. (2008). Long-term process-based morphological modeling of the Marsdiep tidal basin. *Marine Geology*, *256*(1–4), 90–100. https://doi.org/10.1016/j.margeo.2008.10.003

de Glopper, R. J. (1967). *Over de bodemgesteldheid van het waddengebied* (pp. 5–61). Van zee tot land.

de Vet, P. L. M., van Prooijen, B. C., Schrijvershof, R. A., van der Werf, J. J., Ysebaert, T., Schrijver, M. C., & Wang, Z. B. (2018). The importance of combined tidal and meteorological forces for the flow and sediment transport on intertidal shoals. *Journal of Geophysical Research: Earth Surface*. https://doi.org/10.1029/2018JF004605

Dijkstra, Y. M., Schuttelaars, H. M., & Schramkowski, G. P. (2019). A regime shift from low to high sediment concentrations in a tide-dominated estuary. *Geophysical Research Letters*, *46*(8), 4338–4345. https://doi.org/10.1029/2019GL082302

Dissanayake, D. M., Roelvink, J. A., & van der Wegen, M. (2009). Modelled channel patterns in a schematized tidal inlet. *Coastal Engineering*, *56*(11–12), 1069–1083. https://doi.org/10.1016/j.coastaleng.2009.08.008

Edmonds, D. A., Paola, C., Hoyal, D. C., & Sheets, B. A. (2011). Quantitative metrics that describe river deltas and their channel networks. *Journal of Geophysical Research*, *116*(4), 1–15. https://doi.org/10.1029/2010JF001955

Edmonds, D. A., & Slingerland, R. L. (2010). Significant effect of sediment cohesion on deltamorphology. *Nature Geoscience*, *3*(2), 105–109. https://doi.org/10.1038/ngeo730

Elmilady, H., van der Wegen, M., Roelvink, D., & van der Spek, A. (2020). Morphodynamic evolution of a fringing sandy shoal: From tidal levees to sea level rise. *Journal of Geophysical Research: Earth Surface*, *125*(6), 1–21. https://doi.org/10.1029/2019JF005397

Elmilady, H., Wegen, M., Roelvink, D., & Spek, A. (2022). Modeling the morphodynamic response of estuarine intertidal shoals to sea-level rise. *Journal of Geophysical Research: Earth Surface*, *127*(1). https://doi.org/10.1029/2021JF006152

Galiforni-Silva, F., Wijnberg, K. M., & Hulscher, S. J. (2020). Storm-induced sediment supply to coastal dunes on sand flats. *Earth Surface Dynamics*, *8*(2), 335–350. https://doi.org/10.5194/esurf-8-335-2020

Geleynse, N., Storms, J. E., Walstra, D. J. R., Jagers, H. R., Wang, Z. B., & Stive, M. J. (2011). Controls on river delta formation; insights from numerical modelling. *Earth and Planetary Science Letters*, *302*(1–2), 217–226. https://doi.org/10.1016/j.epsl.2010.12.013

Grabowski, R. C., Droppo, I. G., & Wharton, G. (2011). Erodibility of cohesive sediment: The importance of sediment properties. *Earth-Science Reviews*, *105*(3–4), 101–120. https://doi.org/10.1016/j.earscirev.2011.01.008

Guo, L., van der Wegen, M., Roelvink, D. J., Wang, Z. B., & He, Q. (2015). Long-term, process-based morphodynamic modeling of a fluvio-deltaic system, part I: The role of river discharge. *Continental Shelf Research*, *109*, 95–111. https://doi.org/10.1016/j.csr.2015.09.002

Hajek, E., Edmonds, D., Millard, C., Toms, L., & Fogaren, C. (2012). Records of transient avulsion-related river patterns in ancient deposits: Evidence for different styles of channel-floodplain coupling. In *AGU Fall Meeting Abstracts*.

Herman, P. M., Middelburg, J. J., & Heip, C. H. (2001). Benthic community structure and sediment processes on an intertidal flat: Results from the ECOFLAT project. *Continental Shelf Research*, *21*(18–19), 2055–2071. https://doi.org/10.1016/S0278-4343(01)00042-5

Hibma, A., De Vriend, H. J., & Stive, M. J. (2003). Numerical modelling of shoal pattern formation in well-mixed elongated estuaries. *Estuarine, Coastal and Shelf Science*, *57*(5–6), 981–991. https://doi.org/10.1016/S0272-7714(03)00004-0

Hoitink, A. J., Nittrouer, J. A., Passalacqua, P., Shaw, J. B., Langendoen, E. J., Huismans, Y., & van Maren, D. S. (2020). Resilience of river deltas in the Anthropocene. *Journal of Geophysical Research: Earth Surface*, *125*(3), 1–24. https://doi.org/10.1029/2019JF005201

IPCC. (2022). In H.-O. Pörtner, D. C. Roberts, M. Tignor, E. S. Poloczanska, K. Mintenbeck, & A. Alegr (Eds.), *Climate Change 2022: Impacts, Adaptation and Vulnerability. Contribution of Working Group II to the Sixth Assessment Report of the Intergovernmental Panel on Climate Change*. Cambridge University Press. https://doi.org/10.1017/9781009325844

Jacobs, W. (2011). *Sand-mud erosion from a soil mechanical perspective* (PhD thesis). Delft University of Technology.

Jacobs, W., Le Hir, P., Van Kesteren, W., & Cann, P. (2011). Erosion threshold of sand–mud mixtures. *Continental Shelf Research*, *31*(10), S14–S25. https://doi.org/10.1016/j.csr.2010.05.012

Le Hir, P., Cayocca, F., & Waeles, B. (2011). Dynamics of sand and mud mixtures: A multiprocess-based modelling strategy. *Continental Shelf Research*, *31*(10), S135–S149. https://doi.org/10.1016/j.csr.2010.12.009

Lesser, G. R., Roelvink, J. A., van Kester, J. A., & Stelling, G. S. (2004). Development and validation of a three-dimensional morphological model. *Coastal Engineering*, *51*(8–9), 883–915. https://doi.org/10.1016/j.coastaleng.2004.07.014

Manning, A. J., Baugh, J. V., Spearman, J. R., Pidduck, E. L., & Whitehouse, R. J. (2011). The settling dynamics of flocculating mud-sand mixtures: Part 1—Empirical algorithm development. *Ocean Dynamics*, *61*(2–3), 311–350. https://doi.org/10.1007/s10236-011-0394-7

Marciano, R., Wang, Z. B., Hibma, A., De Vriend, H. J., & Defina, A. (2005). Modeling of channel patterns in short tidal basins. *Journal of Geophysical Research*, *110*(1), 1–13. https://doi.org/10.1029/2003JF000092

Mengual, B., Hir, P. L., Cayocca, F., & Garlan, T. (2017). Modelling fine sediment dynamics: Towards a common erosion law for fine sand, mud and mixtures. *Water*, *9*(8), 564. https://doi.org/10.3390/w9080564

Mitchener, H., & Torfs, H. (1996). Erosion of mud/sand mixtures. *Coastal Engineering*, *29*(1–2), 1–25. https://doi.org/10.1016/s0378-3839(96)00002-6

Oost, A. P. (1995). *Dynamics and sedimentary development, of the Dutch Wadden Sea with emphasis on the Frisian Inlet. A study of the barrier islands, ebb-tidal deltas, inlets and drainage basins* (PhD-thesis). Utrecht University.

Partheniades, E. (1965). Erosion and deposition of cohesive soils. *Journal of the Hydraulics Division*, *91*(1), 105–139. https://doi.org/10.1061/jyceaj.0001165

Rahdarian, A., Bryan, K. R., & Van Der Wegen, M. (2022). On the influence of antecedent morphology on development of equilibrium bathymetry in estuaries past and future. *Journal of Geophysical Research: Earth Surface*, *127*(8), 1–18. https://doi.org/10.1029/2022JF006621

Ridderinkhof, W., de Swart, H. E., van der Vegt, M., Alebregtse, N. C., & Hoekstra, P. (2014). Geometry of tidal inlet systems: A key factor for the net sediment transport in tidal inlets. *Journal of Geophysical Research: Oceans*, *119*(10), 6988–7006. https://doi.org/10.1002/2014JC010226

Rijkswaterstaat. (1998). *Sedimentatlas Waddenzee (CD-Rom)*. Rijksinstituut voor Kust en Zee.

Rijkswaterstaat. (2023). Vaklodingen bathymetry request page [Dataset]. Rijkswaterstaat Ministerie van Infrastructuur en Waterstaat. Retrieved from www.rijkswaterstaat.nl/formulieren/contactformulier-servicedesk-data

Sanford, L. P., & Halka, J. P. (1993). Assessing the paradigm of mutually exclusive erosion and deposition of mud, with examples from upper Chesapeake Bay. *Marine Geology*, *114*(1–2), 37–57. https://doi.org/10.1016/0025-3227(93)90038-W

Schindler, R. J., Parsons, D. R., Ye, L., Hope, J. A., Baas, J. H., Peakall, J., et al. (2015). Sticky stuff: Redefining bedform prediction in modern and ancient environments. *Geology*, *43*(5), 399–402. https://doi.org/10.1130/G36262.1

Schrijvershof, R. A., van Maren, D. S., Torfs, P. J. J. F., & Hoitink, A. J. F. (2023). A synthetic spring-neap tidal cycle for long-term morphodynamic models. *Journal of Geophysical Research: Earth Surface*, *128*(3), e2022JF006799. https://doi.org/10.1029/2022JF006799

Sievers, J., Rubel, M., & Milbradt, P. (2020). *EasyGSH-DB: Themengebiet - Sedimentologie*. Bundesanstalt für Wasserbau. https://doi.org/10.48437/02.2020.K2.7000.0005

Soulsby, R. L., & Clarke, S. (2005). Bed shear-stresses under combined waves and currents on smooth and rough beds produced within Defra project FD1905 (EstProc) abcd Document Information (Vol. *1905*).

Spearman, J. R., Manning, A. J., & Whitehouse, R. J. (2011). The settling dynamics of flocculating mud and sand mixtures: Part 2—Numerical modelling. *Ocean Dynamics*, *61*(2–3), 351–370. https://doi.org/10.1007/s10236-011-0385-8

Syvitski, J. P., Kettner, A. J., Overeem, I., Hutton, E. W., Hannon, M. T., Brakenridge, G. R., et al. (2009). Sinking deltas due to human activities. *Nature Geoscience*, *2*(10), 681–686. https://doi.org/10.1038/ngeo629

Tejedor, A., Longjas, A., Zaliapin, I., & Foufoula-Georgiou, E. (2015). Delta channel networks: 2. Metrics of topologic and dynamic complexity for delta comparison, physical inference, and vulnerability assessment. *Water Resources Research*, *51*(6), 4019–4045. https://doi.org/10.1002/2014WR016604

Torfs, H. (1995). *Erosion of mud/sand mixtures* (PhD thesis). University of Leuven.

van der Wal, D., Wielemaker-van den Dool, A., & Herman, P. M. (2010). Spatial synchrony in intertidal benthic algal biomass in temperate coastal and estuarine ecosystems. *Ecosystems*, *13*(2), 338–351. https://doi.org/10.1007/s10021-010-9322-9

van der Wegen, M., & Roelvink, J. A. (2008). Long-term morphodynamic evolution of a tidal embayment using a two-dimensional, process-based model. *Journal of Geophysical Research*, *113*(C3), C03016. https://doi.org/10.1029/2006JC003983

van Kessel, T., Spruyt-de Boer, A., van der Werf, J., Sittoni, L., van Prooijen, B. C., & Winterwerp, H. (2012). Bed module for sand-mud mixtures. *Deltares Report 1200327-000-ZKS-0013*.

van Ledden, M. (2003). *Sand-mud segregation in estuaries and tidal basins* (PhD thesis). Delft University of Technology.

van Ledden, M., van Kesteren, W. G., & Winterwerp, J. C. (2004). A conceptual framework for the erosion behaviour of sand-mud mixtures. *Continental Shelf Research*, *24*(1), 1–11. https://doi.org/10.1016/j.csr.2003.09.002

van Ledden, M., Wang, Z. B., Winterwerp, H., & de Vriend, H. (2004). Sand-mud morphodynamics in a short tidal basin. *Ocean Dynamics*, *54*(3–4), 385–391. https://doi.org/10.1007/s10236-003-0050-y

van Ledden, M., Wang, Z. B., Winterwerp, H., & de Vriend, H. (2006). Modelling sand-mud morphodynamics in the Friesche Zeegat. *Ocean Dynamics*, *56*(3–4), 248–265. https://doi.org/10.1007/s10236-005-0055-9

van Rijn, L. C. (1993). *Principles of sediment transport in rivers, estuaries and coastal seas*. Aqua Publications.

van Rijn, L. C. (2020). Erodibility of mud-sand bed mixtures. *Journal of Hydraulic Engineering*, *146*(1), 1–19. https://doi.org/10.1061/(ASCE)HY.1943-7900.0001677

Wang, Z. B., van Maren, D. S., Ding, P. X., Yang, S. L., van Prooijen, B. C., de Vet, P., et al. (2015). Human impacts on morphodynamic thresholds in estuarine systems. *Continental Shelf Research*, *111*, 174–183. https://doi.org/10.1016/j.csr.2015.08.009

Winterwerp, J. C. (2007). On the sedimentation rate of cohesive sediment. In *Paper presented at 7th International Conference on Estuarine and Coastal Fine Sediments Dynamics, Gloucester Point, Virginia, USA* (Vol. 8, pp. 209–226). Elsevier B.V. https://doi.org/10.1016/S1568-2692(07)80014-3

Winterwerp, J. C., van Kessel, T., van Maren, D. S., & van Prooijen, B. C. (2021). *Fine sediment in open water: From fundamentals to modeling* (Vol. 55). World Scientific. https://doi.org/10.1142/12473

Winterwerp, J. C., & van Kesteren, W. G. M. (2004). *Introduction to the physics of cohesive sediment in the marine environment*. Elsevier.

Yao, P., Hu, Z., Su, M., Chen, Y., & Ou, S. (2018). Erosion behavior of sand-silt mixtures: The role of silt content. *Journal of Coastal Research*, *85*, 1171–1175. https://doi.org/10.2112/SI85-235.1

Zhou, Z., Liu, Q., Fan, D., Coco, G., Gong, Z., Möller, I., et al. (2021). Simulating the role of tides and sediment characteristics on tidal flat sorting and bedding dynamics. *Earth Surface Processes and Landforms*, *46*(11), 2163–2176. https://doi.org/10.1002/esp.5166

Zhou, Z., Wu, Y., Fan, D., Wu, G., Luo, F., Yao, P., et al. (2022). Sediment sorting and bedding dynamics of tidal flat wetlands: Modeling the signature of storms. *Journal of Hydrology*, *610*, 127913. https://doi.org/10.1016/j.jhydrol.2022.127913